



# Impact of a regional fault zone on the properties of a deep geothermal carbonate reservoir unit (Devonian of NRW)

Chelsea Pederson<sup>1</sup>, Mathias Mueller<sup>1</sup>, Kevin Lippert<sup>1,2</sup>, Onyedika Anthony Igbokwe<sup>1,3</sup>,  
Sylvia Riechelmann<sup>1</sup>, Sven Lersch<sup>1</sup>, Peter Benger<sup>1</sup>, Alessandro Verdecchia<sup>1</sup> &  
Adrian Immenhauser<sup>1, 2\*</sup>

Pederson, C., Mueller, M., Lippert, K., Igbokwe, O. A., Riechelmann, S., Lersch, S., Benger, P., Verdecchia, A. & Immenhauser, A. (2021): Impact of a regional fault zone on the properties of a deep geothermal carbonate reservoir unit (Devonian of NRW). – Z. Dt. Ges. Geowiss., 172: 339–364, Stuttgart.

**Abstract:** A multi-proxy field and laboratory study was conducted to investigate the impact of a regional fault zone on Devonian carbonate geothermal reservoir properties. The outcrop analogue chosen is exposed in the Steltenberg quarry (North Rhine-Westphalia, Germany) and provides access to Devonian lime- and dolostone units affected by branches of the Ennepe Thrust Fault zone. Data presented include (i) field evidence from sedimentological and structural data, (ii) petrographic and mineralogical analyses, and (iii) geochemical and petrophysical data. Although the interpretation of the depositional environment is not trivial, the carbonate facies present generally reflect the shedding of reefal material from large bioherms to the west of the study areas as well as localised, small bioherms prone to storm disintegration. The inherited properties of these carbonates at deposition, and a clear understanding of their diagenetic history, are the prerequisite for extrapolation between outcrop analogues and their corresponding subsurface units. We document a detailed interpretation of the paragenetic sequence that affected these rocks from deposition, burial, subsequent hydrothermal overprint related to rock disintegration and fluid circulation along the fault zone, and finally, late-stage meteoric overprint. Emphasis is placed on various forms of dolomitisation and its effect on rock properties and reservoir quality. The resulting scenario is complex, and when comparing the data from the Steltenberg quarry with nearby outcrops, significant regional heterogeneity is observed. It is important to separate between: (i) diffuse, locally distributed dolomitisation, (ii) replacive dolomitisation (fronts), spatially separating lime- and dolostones, and (iii) fault-bound, hydrothermal dolomitisation. The Devonian carbonates in the Steltenberg quarry examined here have higher thermal conductivity compared to the Jurassic (Malm) carbonate units in the Munich area, with some even higher than the values of massive limestone facies of the Munich area. As a large portion of North Rhine-Westphalia's territory is underlain by Devonian carbonates, this is considered significant. However, emphasis is placed on the fact, that data shown here document the spatially complex organisation of rock types and their reservoir properties. This presents a warning against oversimplifications when extrapolating observations from outcrops into subsurface rock bodies.

**Keywords:** carbonates, geothermal, energy production, geochemistry, petrophysics, outcrop study, hydrothermal alteration

## 1. Introduction

### 1.1 Carbonate rock bodies as deep hydrothermal reservoir facies in North Rhine-Westphalia

Deep-geothermal applications have the potential to provide sustainable energy for district heating systems in urban regions. In Germany, this technology is presently applied in

the city of Munich, where heat from deep, karstified carbonate reservoirs is exploited (Dirner & Steiner 2015). According to the long-term energy supply plan of the public services in Munich, heat extracted from deep geothermal reservoirs is intended to provide 100% of the necessary thermal energy by the year 2040 (Wissing 2009).

A large portion of North Rhine-Westphalia's (NRW) territory is underlain by Devonian carbonate rocks, most of which are located at burial depths between some hundreds

\*Addresses of the authors:

<sup>1</sup>Institute for Geology, Mineralogy and Geophysics, Ruhr-Universität Bochum, Universitätsstr. 150, 44801 Bochum, Germany (chelsea.pederson@rub.de)

<sup>2</sup>Fraunhofer Research Institution for Energy Infrastructures and Geothermal Systems IEG, Am Hochschulcampus 1, 44801 Bochum, Germany

<sup>3</sup>Department of Physics, Geology and Geophysics, Alex Ekwueme Federal University Ndufu Alike, Ikwo, P.M.B. 1010, Abakaliki, Ebonyi State, Nigeria

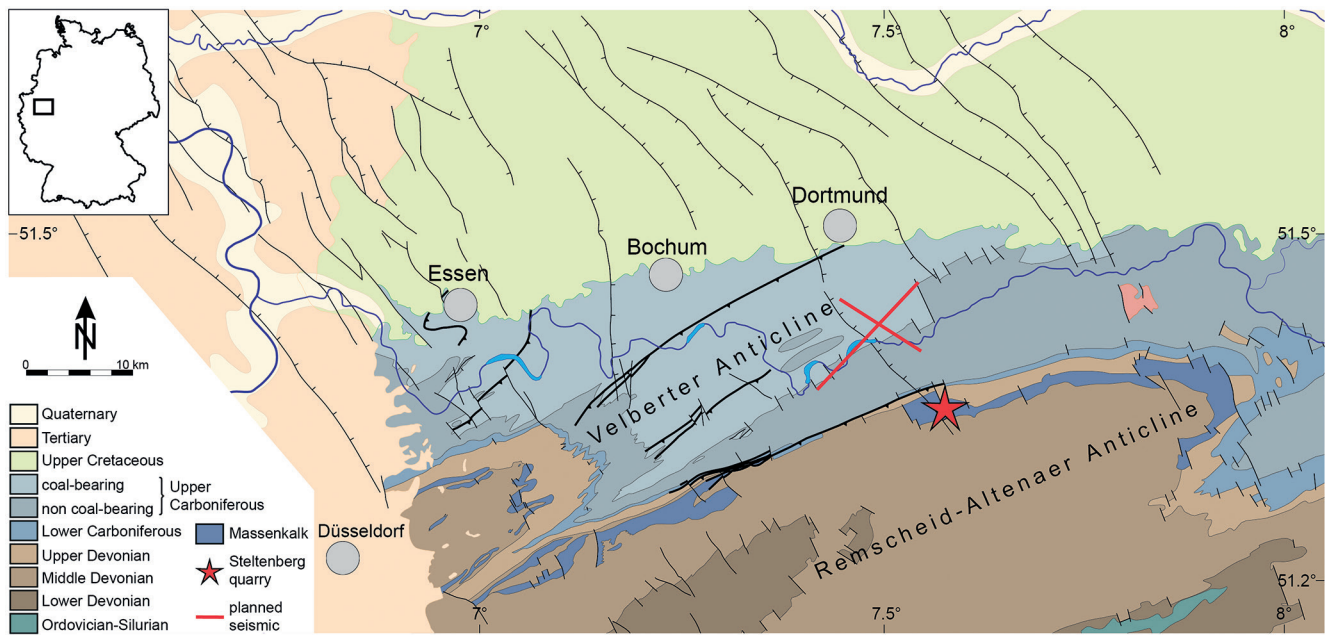


**Fig. 1:** Geological map of the northern Rhenish Massif. The studied outcrop in the Devonian Massenkalk is indicated by a red star (modified from Götte 2004).

and several thousands of metres (Franke et al. 1990; Krebs 1974; Lippert et al. 2019). Recently, these units have become a major research focus due to their stratigraphic thickness (up to 1,300 m), their position beneath the most populated and industrialised areas of NRW, and their potential as deep geothermal reservoirs (Balcewicz et al. 2021; Lippert et al. 2019; Thiel 2018). The significance of the deep geothermal Devonian carbonate reservoirs in NRW is based on their potential as industrial thermal energy supply and district-heating reservoirs. The aim is to convert the existing heating system in the Ruhr metropolitan area – one of Europe’s largest district-heating networks with a total length of 4,300 km – from a primarily coal-fuelled system to a geothermal one. As the Ruhr metropolitan area includes 50 cities with over 5 million people living within an area of approximately 4,400 km<sup>2</sup> (Knutzen et al. 2015), this conversion to environmentally sustainable heat is of great environmental significance.

Several case studies with the aim to work towards this larger goal exist. One case study referred to as the “Kabel Zero project” (<https://www.ieg.fraunhofer.de/en/references/geothermal-paper-drying.html>) is an interdisciplinary approach with the goal to evaluate the deep geothermal reservoir potential of the Devonian carbonate units of the Rhenish Massif in NRW. Here, geothermal heat is intended to substitute for natural-gas operated combined heat and power (CHP) generation plants to provide process steam for a paper factory located in the northern part of the city of Hagen. According to the Geological Survey of North Rhine-Westphalia, the subsurface in this area is characterised by Devonian carbonate rocks, located at depths between 3,200 and 4,100 m below the surface (Salamon et al. 2020). A seismic survey is

currently under way to validate this claim (Fig. 1). Outcrops of Devonian carbonate rocks east of the Rhine River are located in the southern Ruhr area on the northern flank of the Remscheid-Altener Anticline as well as on the edges of the Velbert Anticline (Fig. 1; Federal Agency for Cartography and Geodesy 2020). The present study focuses on exposed units in one of these quarries.

## 1.2 Evaluating complex, three-dimensional carbonate rock bodies in the subsurface

Despite significant potential, the exploitation of deep geothermal energy is challenging in many ways. Carbonate reservoirs at depth are highly heterogeneous across all scales (from pore- to field-scale), rendering it difficult to predict flow behaviour in the subsurface. Consequently, carbonate reservoir characterisation is associated with a high degree of uncertainty (Grammer et al. 2004). Depositional rock properties of carbonates – as found millions of years later in subsurface rock bodies – is defined by a multitude of biogenic and abiogenic, hydrodynamic and environmental parameters (Dunham 1962; Bjørlykke 2014). During subsequent burial, carbonates undergo significant degrees of alteration (diagenesis) driven by disequilibrium processes between pore fluids and minerals, resulting in dissolution-precipitation processes that often involve mineral fluxes (Swart 2015). These processes have the potential to profoundly alter the mineralogical and chemical characteristics of a given carbonate (Pederson et al. 2020), as well as affect its petrophysical properties (Eberli et al. 2003; Weydt et al. 2018). Compaction often occurs as a consequence of vertical stress during

burial. In order to achieve significant pore-volume reduction, dewatering and plastic or brittle grain deformation is required. Compaction is one of the key parameters controlling rock-fluid volumes at depth, and hence, the type and magnitude of alteration. During compaction, the system gradually changes from a fluid-dominated (fluid-filled, open porosity) to a rock-dominated (fluid-lean) system.

### 1.3 Relevance of facies architecture, diagenesis, regional fault zones and fracture networks

At some hundreds of metres burial depth, mechanical compaction gives way to chemical compaction (Shinn & Robbin 1983), a feature often observed by dissolution seams. Mineralogical changes such as hydrothermal dolomitisation of calcitic and aragonitic carbonates in the subsurface can either occlude or create pore networks (often referred to as “matrix porosity”). Later stages of dedolomitisation or silica cementation add further complexity. These changes are in addition to facies architecture and inherent heterogeneity between various layered units, particularly evident in carbonate strata. Along with vertical stress induced by burial, horizontal, and oblique stress fields related to compressive or extensive tectonism, induces fracturing and jointing of carbonates, a process controlled by rock properties (Mueller 2020). Well-lithified (brittle) limestones may undergo extensive fracturing (here referred to as “fracture porosity”), while more argillaceous marly facies may form impermeable units or flow baffles (Gunter et al. 1997; Ti et al. 1995). Fractures may be spatially distributed or present as fracture corridors. Whether the fracture sets are bound by existing strata, or cross cut various layers can be especially important for indications of fluid flow between various carbonate units (Meier et al. 2017). Moreover, aspects such as fracture lengths and aspect ratios (height to length) are relevant when considering subsurface fluid flow. While open fractures may act as fluid pathways, closed fractures often act as barriers (Maxwell et al. 2011). Large-scale structural features (fault zones) are a case on their own, and are associated with slip surfaces, shearing, and heterogeneous strain distribution, sometimes over km scales (Mueller et al. 2020; Yielding et al. 1999).

Large fault zones are structurally anisotropic discontinuities in the upper crust, which accommodate heterogeneous lithology and strain distribution over a wide range of scales (metres to kilometres; Agosta et al. 2012; Choi et al. 2016; Kim et al. 2004) and form primary controls on reservoirs fluid flow (Caine et al. 1996; Jourde et al. 2002). An established fault zone contains: (i) a fault core (with a breccia and/or a cataclastite), where most of the displacement occurs, and the pre-existing sedimentary and tectonic structures are primarily destroyed, and (ii) an associated damage zone, which is mechanically related to the growth of the fault zone (Agosta & Aydin 2006; Billi et al. 2003; Caine et al. 1996; Chester & Logan 1986; Igbokwe et al. 2020; Sibson 1977). In the damage zone, fault-related fracture networks crosscut the

host rock and depositional structural, including fractures and/or small-scale faults that do not destroy host rock fabrics, may be preserved to variable degrees. Depending on the volume percentage of the fault core and damage zone, and the inherent variability in grain size and fracture permeability, the fault zone may act as a conduit for fluids, a barrier, or a combined conduit-barrier system (Caine et al. 1996; Jourde et al. 2002). In addition, when faults are critically stressed, they become hydraulically conductive, having high permeability (Townend & Zoback 2000). Both the fault core and damage zone are bounded by the host rock, which is frequently characterised by background tectonic structures due to the previous deformation.

Fault zones in NRW are common features that transect hydrothermal reservoirs (Balcewicz et al. 2021; Lippert et al. 2019; Thiel 2018) and are thought to act as both lateral and vertical fluid pathways. Hydrothermal fluids migrate both upward and laterally within fault zones, and may induce significant mineralisation. To address the challenges related to deep geothermal energy, feasibility studies on time-equivalent units in outcrop are extremely helpful when performed with an understanding of the comparability of outcrop versus buried carbonate deposits. The investigation of outcrop analogues is a key tool for the improvement of carbonate reservoir characterisation and modelling of subsurface migration of geothermal fluids (Barbier et al. 2012). Outcrop studies provide insight to the distribution and morphology of geologic bodies and their rock properties across a broad range of scales, from tens-of-kilometre- down to micrometre-scale features. Regarding deep geothermal reservoirs, outcrop analogue studies have been performed to evaluate the potential of the Jurassic (Malm) carbonates in the Munich area (Homuth 2014; Homuth et al. 2014).

### 1.4 Relevance of outcrop studies and applicability of outcrop data to the subsurface

This study evaluates a Devonian carbonate outcrop in the Steltenberg quarry operated by the Hohenlimburger Kalkwerke GmbH (Hagen-Hohenlimburg, NRW), which is an outcrop analogue for a deep geothermal reservoir in the region (Federal Agency for Cartography and Geodesy 2020; Fig. 1). A specific focus is on a regional fault zone and its effect on the host lithologies. This work is highly relevant as no well-logs or cores of the Devonian carbonates at greater depths exist in the study area, and extremely scarce and generally difficult to access within NRW. The approach included: (i) field analysis and sampling of suitable geothermal reservoir lithologies; (ii) measurement of structural data and quantification of the fault core and damage zone properties; and (iii) the analysis of geochemical and petrophysical properties. The aim of this paper is to document the outcome of the outcrop analogue study. By doing so, it is intended to provide an accurate characterisation of reservoir architecture, diagenetic evolution and deformation of the Devonian carbonate units that is critical for the accurate modelling of carbonate reservoirs, and predicting flow behaviour in deep

geothermal reservoirs. A limitation of outcrop studies involved differential processes which have affected the rocks observed at the outcrop and those found in the subsurface. Especially when the target lithology is at great depths (such as the Devonian carbonates of NRW) the mechanical and chemical processes during burial cannot be replicated or extrapolated to the units found at the surface and vice versa (see previous section for further details on stresses and alteration during burial). Work shown here has relevance for those in both the scientific and industrial realms interested in geothermal energy, reservoir characteristics and carbonate diagenesis.

## 2. Regional geotectonic setting

The Steltenberg quarry is located at the northern margin of the Remscheid-Altena Anticline, which belongs to the Rhenish Massif of North Rhine-Westphalia (NRW), Germany (Fig. 1). The position of the Rhenish Massif during the Devonian was near the coast and on the open shelf south of the Old Red continent. During the Early to Middle Devonian, the depositional environment was dominantly shallow marine to deltaic siliciclastic, while the late Middle Devonian primarily comprised carbonate reefs development at the shelf edge and the open shelf. These carbonates form the massive limestone “Massenkalk” unit (Fig. 1), and are not necessarily deposited in reefal environments. Following previous work (Frech 1888; Kayser 1907; Paeckelmann 1913; Krebs 1967), Krebs (1974) developed a depositional facies classification for the Devonian carbonates, specifically the three main facies types: Schwelm, Dorp and Iberg facies.

The Schwelm Facies is a bank or platform unit, which often forms the lower portion of the Middle Devonian carbonate sequence. This facies contains non-wave-resistant stromatoporoids and coral-reef structures, which resulted in a flat, biostromal environment. Distinctive features include a dark colouration, a dense matrix, and a broad variety of poorly-sorted angular fossils due to the low energy depositional environment (Krebs 1967, 1974).

The Dorp Facies represents carbonates with clear influences of biohermal reef buildups that formed locally during the early Late Devonian. This facies can be subdivided into a back-reef environment, the reef-core, and the seaward high-energy fore-reef environment. The Dorp Facies consists of sparry calcite matrix (rather than calcitic-micritic matrix such as in the Schwelm Facies) and shows evidence of high energy depositional environments (Krebs 1967, 1974).

The Iberg Facies consists of grey, sparry, crinoid-brachiopod limestone and typifies the convex caps of the former reef-sections. Here, the typical Devonian reef-building organisms, such as stromatoporoids are absent and replaced by tabulate corals (Burchette 1981). Deposited after the Dorp Facies, the Iberg Facies formed during the Late Devonian in low energy depositional environments below wave base due to an increase in subsidence (Krebs 1974). Additionally, the

reduced thickness (up to a few tens of metres) differentiates the Iberg from the Dorp Facies.

The Devonian carbonate factories were active until the early Late Devonian. Afterwards, sediment deposition was again dominated by siliciclastics (Krebs 1974; Heseemann 1975). The Variscan Orogeny during the Carboniferous led to extensive folding and faulting in the area (Oncken 1988; Fig. 1), during which hydrothermal mineralisation of the Rhenish Massif resulted in intensive dolomitisation of the massive limestone units (Kimbauer 1998; Richter 2000; Gillhaus et al. 2003). The exposed units in the Steltenberg quarry are primarily massive upper Middle Devonian carbonates (Givetian; Koch-Früchtl & Früchtl 1993) with varying extents of dolomitisation. Two main fault types occur in the neighbouring region of the Steltenberg quarry, which may have caused secondary alteration of the Devonian units. Near-perpendicular (with respect to the quarry orientation) fractures also create networks in the Devonian carbonates along the northern margin of the Remscheid-Altena Anticline. These are capable of forming interconnected, permeable units with geothermal reservoir potential. The first main fracture orientation is WSW–ENE-striking thrusts, such as the Ennepe-Thrust (Oncken 1988). Although the main strand of the Ennepe-Thrust Fault does not cross the Steltenberg quarry, the branches of this nearby system are partly responsible for the fracturing of the carbonates in the quarry. The second main type of faults in the study area is a NNW–SSE striking system of post-Variscan age normal faults, such as the “Großholthausener Sprung” or the “Rüdinghausener Sprung” (Gillhaus et al. 2003). These normal faults represent reactivated extensional structures that formed perpendicularly to the strike of the fold belt at the end of the Palaeozoic due to crustal uplift and stretching until the Givetian, prior to the Variscan Orogeny. During that time, a clockwise rotation of the compressive stress field caused a NNW–SSE extension. While the direction of this extensional regime changed slightly, this stress still exists in the present (Oncken 1988).

The Devonian carbonates of the northern part of the Rhenish Massif near the study area were buried to maximum depth of about 6,500 m during the later stages of the Variscan Orogeny, roughly 300 Ma ago. Since the Permian (Zechstein), the Palaeozoic pre- and syn-Variscan sediments of the region have been uplifted, and thus cooled, while overburden thicknesses of 4,000–5,500 m have been eroded in the study area (Littke et al. 2000).

## 3. Methodology

### 3.1 Fieldwork

The Devonian Massenkalk in the Steltenberg quarry was the chosen target for this study due to its high variety of strata, ranging from well-preserved limestones to various types of dolostones. Moreover, the Devonian geological and tectonic framework in this region is well-established (Gillhaus et al. 2003; Götte 2004 and references therein). To assess the spa-

tial variability of the diagenetic and tectonic impact on petro-physical, petrographic, and geochemical data, and hence, corresponding geothermal reservoir properties, our sampling strategy was as follows: (i) samples were collected throughout the quarry to assess the complete paragenetic succession and their geochemical composition for the reconstruction of palaeo-fluid flow and its relation to fault zone overprint; (ii) a suite of representative rock types from less disturbed sedimentary rocks to highly-overprinted facies was collected for petrophysical analyses and facies determination; (iii) a stratigraphic section was logged, with corresponding sample collection (5 m resolution) along a 310 m long transect on the fifth sole to assess any spatial difference in alteration features relative to the fault zone.

### 3.2 Fault zone analysis and connectivity

Fracture analysis was performed in the field on selected outcrops within the Steltenberg quarry. The data were acquired by (i) direct measurement of fractures in the area, and (ii) ortho-rectified photographs (using a Nikon P7800 camera) with >96% photo overlap (% of overlap = area of intersection/area of union  $\times$  100). Fractures were structurally characterised and classified based on structural complexity. Structural data were collected for faults exposed along the quarry, including fault plane orientations and apparent fault displacements. The high-resolution outcrop images were then merged, imported and georeferenced in ArcGIS where the fracture networks linked with the fault zone were digitised for further geometric, kinematic and topological analysis (e.g. Igbokwe et al. 2020; Nyberg et al. 2018). The topological analysis was performed on the digitised fault zones to distinguish the fault network and to constrain connectivity. Topology determines the geometric relationship between fractures and demonstrates the arrangement of fractures to assess their connectivity. In 2D, the topology of fractures consists of nodes and branches between nodes. Three types of nodes and branches are recognised: I-, Y-, X-nodes, and II-, IC-, CC-branches (for a detailed classification and mathematical derivation see Manzocchi 2002; Sanderson & Nixon 2015; Sanderson & Nixon 2018). The proportion of different nodes and branch types defines the network topology, and when plotted on a ternary diagram permits the assessment of several fracture networks.

### 3.3 Petrophysics

Petrophysical parameters such as thermal conductivity, porosity and permeability exhibit direct effects on reservoir potential and play a very significant role in their overall assessment (Homuth 2014; Homuth et al. 2015a; Homuth et al. 2015b; Bohnsack et al. 2020). Because carbonate facies type can have an extremely pronounced impact on their petrophysical parameters compared to pressure and temperature associated to burial depth (Stober 2014), the petrophysical analyses performed in this study were facies related. To fa-

cilitate the comparison of different facies, only matrix properties were evaluated in order to clarify relative statements about the geothermal reservoir potential of the different facies. Due to the large effect of mineralogy on the thermal and particularly hydraulic properties of carbonates compared to the depositional facies, interpretations in this study were based on dolomite content, resulting in the following mineralogical facies types: limestone (<20% dolomite), dolomitic limestone (20–75% dolomite) and dolostone (75–100% dolomite). Reservoir potential can be hypothesised by comparing petrophysical results to outcrop data, such as in studies of the Upper Jurassic carbonates near Munich (Dirmer & Steiner 2015; Weydt et al. 2018). Bulk XRD measurements were conducted for every specimen ( $n = 33$ ) prior to petrophysical analysis.

Thermal conductivity ( $\lambda$ ) highly depends on the mineralogy, structure, density, pore volume, and amount of cracks in a sample, and provides insight to conductive subsurface heat transfer properties (Kaltschmitt et al. 2006), making it an important parameter for evaluating geothermal reservoir potential. Thermal conductivity is measured using a Thermal Conductivity Scanner (TCS), which is a semi-automatic apparatus for a contactless determination of thermal conductivity (Popov et al. 1983).

Total and effective porosity of the mineralogical facies types helps elucidate thermal water storage and transport potential in the subsurface. While total porosity ( $\varphi_{tot}$ ) represents the overall pore volume within a rock volume, effective porosity ( $\varphi_{eff}$ ) depicts the connected pore space within a sample. Bulk and grain densities ( $\rho_{bulk}$  and  $\rho_{grain}$ ) were first determined to calculate total porosity. The bulk density is identified by simple weighing and geometrical measuring steps, while grain density is determined by pycnometer (Gay-Lussac pycnometers; 101.156 and 25.299 ml) tests according to the DIN ISO 18124 (2019) for removing pore space prior to determining the mass. Total porosity is subsequently determined from  $\rho_{bulk}$  and  $\rho_{grain}$  according to Manger (1963). Effective porosity ( $\varphi_{eff}$ ) is calculated by the following equation:

$$\varphi_{eff} = 100 \times \left( \frac{\Delta m / \rho_w}{V} \right) \quad \text{Eq. 1}$$

wherein  $\rho_w$  represents the density of the pore-filling fluid and  $\Delta m$  is the difference in mass of the sample core between dry and saturated states. Cores were considered “dry” following drying in an oven at 60 °C for 24 hrs and allowed to cool to room temperature in ambient laboratory conditions.

The most direct way to determine hydraulic conductivity is by measuring the permeability ( $k$ ), which is proportional to  $\varphi_{eff}$  (Tan et al. 2017). Permeability measurements were performed in a Hoek cell, which administers triaxial pressure on a short core sample. Equal axial and confining pressures of 10 MPa were used. A Teledyne Isco pump system was connected to the lower axial permeability cap of the cell, which is in contact with the top of the sample (diameter = 40 mm, length = 85 mm), and forces deionised water through the sample. Parameters used include runs at 30, 60, and 90% of the confining and axial pressures (here, 3, 6, and 9 MPa)

to determine the permeability. The upper axial permeability cap in contact with the opposite end of the sample is not connected to the pump system, resulting in a constant outflow pressure of 0.1 MPa. Final permeability ( $K$ ) is calculated using Darcy's law (Darcy 1856), which considers the volumetric fluid flow through the sample core ( $Q$ ), the dynamic viscosity of the fluid ( $\eta$ ), the length ( $l$ ) and the cross-sectional surface area ( $A$ ) perpendicular to the sample, and the pressure difference between in- and outflow ( $\Delta\rho$ ), as in the following equation:

$$K = \frac{\eta \times Q \times l}{A \times \Delta\rho} \quad \text{Eq. 2}$$

### 3.4 Petrography

#### Depositional facies analysis

Eleven thin sections from macroscopically distinguishable rock sections and corresponding facies were analysed using a Zeiss polarising microscope (Axio Scope A1) to determine depositional facies. The most important parameters for differentiating between the depositional facies described in section 3.2 were the fossil or allochem content, the mineralogy, and the porosity. To determine the mineralogical composition, the thin sections were partially stained with Alizarin-Red-S, which differentiates calcite from other mineral phases. If calcite is present, the thin section minerals appear reddish, while dolomite or other minerals do not react.

#### Cement stratigraphy

To determine the cement stratigraphy, polished thin sections were analysed using both polarised and cathodoluminescence microscopy. Polarised images were taken on a Leica DM4500P microscope (Leica Microsystems GmbH, Wetzlar, Germany). Cathodoluminescence analyses were performed using a hot cathode (HC1-LM) facility at the Ruhr-University Bochum (Neuser et al. 1996) equipped with a DC73 camera system (Olympus). Thin sections were sputter coated with a 15 nm thick gold layer to avoid charging. The electron beam had an acceleration voltage of the 14 kV, a current density from 5 to 10  $\mu\text{A}/\text{mm}^2$ , and a beam current from 0.1–0.2 mA. Dolomite and calcite cement phases were identified based on luminescence colours (following Bruckschen & Richter 1993) and textural criteria. By evaluating the various cement phases in relation to each other, a paragenetic sequence, from earliest to latest precipitates, was developed. For further details on cement stratigraphy using cathodoluminescence microscopy, see Bruckschen et al. (1992); Bruckschen & Richter (1993) and Richter et al. (2003).

### 3.5 Geochemistry

Mineralogy of hand specimens from the stratigraphic section, and individual cement phases was analysed using powder X-Ray Diffraction (PXRD). To quantify the minerals

present, 70–100 mg of powder was drilled from the samples with a handheld Dremel. Sampling locations within individual phases were based on previous petrographic evaluation using normal, polarised and cathodoluminescence microscopy. Sample powders were homogeneously distributed on a silicon sample carrier, before mounting and aligning them on a rotating goniometer head. Measurements were performed on a PANalytical Empyrean diffractometer using copper radiation ( $\lambda = 0.154 \text{ \AA}$ ) equipped with a PIXcel1D detector (Medipix2 collaboration, Ruhr-University, Bochum, Germany). Scanning range of 2-Theta was 5 to 80°, with a step size of 0.0131°, and a duration of 598.9 ms. Phases were identified using the software X'Pert HighScore Plus (PANalytical B.V.).

Element concentrations, carbon- and oxygen-isotope values ( $\delta^{13}\text{C}$  and  $\delta^{18}\text{O}$ ), and  $^{87}\text{Sr}/^{86}\text{Sr}$  ratios were analysed at Ruhr-University Bochum. For  $\delta^{13}\text{C}$  and  $\delta^{18}\text{O}$  analysis, 90–110  $\mu\text{g}$  of carbonate sample powder was reacted with phosphoric acid at 70 °C before analysis. Isotope values were determined using a MAT 253 (Thermo Fisher Scientific) continuous flow isotope ratio mass spectrometer (CF-IRMS) coupled with a ConFloIV and a GasBenchII. Values are reported in‰ relative to the VPDB standard. Measurement error is reported as 1 $\sigma$  standard deviation (SD). The certified standards IAEA-603 and NBS 18 were used for data correction. The 1 $\sigma$ -reproducibility of the internal limestone standard was 0.05‰ for  $\delta^{13}\text{C}$  and 0.08‰ for  $\delta^{18}\text{O}$  ( $n = 235$ , 2019–2020) and 0.06‰ for  $\delta^{13}\text{C}$  and 0.16‰ for  $\delta^{18}\text{O}$  ( $n=80$ , 2019–2020) for the internal dolomite standard.

Elemental concentrations (Ca, Mg, Sr, Fe, Mn) were measured on three representative samples from the stratigraphic section – one in the Massenkalk unit (depth of 0 m in the measured section), one in the heart of the fault zone (depth of 140 m in the measured section), and one on the far side of the fault zone (depth of 300 m in the measured section). Samples were run by dissolving approximately 1.5 mg of sample powder in 1 ml 3M  $\text{HNO}_3$  for 24 h at room temperature before diluted with 2 ml deionised water. Concentrations were determined by inductively coupled plasma optical emission spectrometry (ICP-OES, iCAP 6500 DUO, Thermo Fisher Scientific). Measurement error is reported as 1 $\sigma$  standard deviation (SD). The long-term 1 $\sigma$ -reproducibility of the certified standards BCS-CRM512 (dolomite; Bureau of Analysed Samples Ltd) and BCS-CRM513 (limestone; Bureau of Analysed Samples Ltd) is 0.3 wt.% and 0.6 wt.% for Ca, 0.2 wt.% and 0.002 wt.% for Mg, 0.002 wt.% and 0.0002 wt.% for Sr, 0.001 wt.% and 0.0009 wt.% for Fe, and 0.0001 wt.% and 0.0002 wt.% for Mn, respectively ( $n = 116$ ; 2019–2020).

Strontium-isotope ratio analyses were performed by dissolving between 0.3 to 16.3 mg (to receive a Sr content of 400 ng per sample) of sample powder in 1 ml 6M HCl and dried on a hot plate at 90 °C before being re-dissolved in 0.4 ml 3M  $\text{HNO}_3$ . PFA columns filled with TrisKem Sr ion exchange resin (100–150 mesh) were used to collect the Sr fraction with 2 ml of deionised water. Subsequently, samples are dried on a hot plate at 90 °C and re-dissolved in 1 ml of a  $\text{H}_2\text{O}_2$ - $\text{HNO}_3$  to remove organic remains. Samples were then

evaporated on a hot plate at 60 °C and re-dissolved in 0.4 ml 6M HCl. After evaporation at 90 °C, samples were re-dissolved in 1 µl of ionisation-enhancing solution (after [Birck 1986](#)) and loaded on Re single filaments. Isotope ( $^{87}\text{Sr}/^{86}\text{Sr}$ ) ratios were analysed by thermal ionisation mass spectrometry (TIMS) TI-BOX (formerly MAT 262; Spectromat). Measurement error is reported as 2σ standard error (SE). The long-term reproducibility of NIST NBS 987 and USGS EN-1 is  $^{87}\text{Sr}/^{86}\text{Sr} = 0.710242 \pm 0.000001$  2σ SE (n = 526) and  $^{87}\text{Sr}/^{86}\text{Sr} = 0.709161 \pm 0.000002$  2σ SE (n = 444), respectively.

## 4. Results

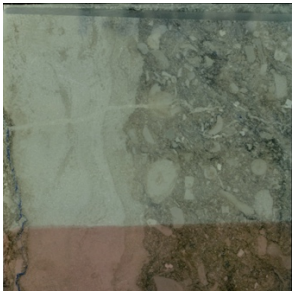
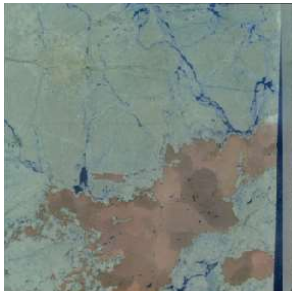
### 4.1 Sedimentology and stratigraphy

The analysis of mineralogical and depositional facies types in the Steltenberg quarry is a fundamental step in assessing the geothermal reservoir potential, as dolomite content determines the petrophysical behaviour of the Devonian carbonates, while the depositional facies helps determine the local formation thickness. Of a total of 33 measured samples, 14 were classified as limestone (<20% dolomite), 8 as dolomitic limestone (20–75% dolomite), and 11 as dolostones (>75% dolomite) according to the mineralogical facies classifica-

tion. Table 1 shows one typical example from each depositional facies type occurring in the quarry – Schwelm (A) and Dorp fore-reef (B) – as well as one dolomitised sample (C) to demonstrate the main differences between the depositional and mineralogical facies. The main distinguishing factors include: carbonate rock type (according to [Dunham 1962](#)), the matrix analysis, porosity characteristics, the allochem content (including both fossil assemblage and non-biogenic constituents) and mineralogy from thin section staining (Table 1). Of the 11 thin sections, 3 belonged to the Schwelm facies, 3 to the hydrothermal dolomite facies, and 5 to the fore-reef Dorp facies.

The facies also change along the measured stratigraphic section (Figs. 2–4). Generalised facies description along the section in relation to the quarry is shown in Fig. 2, with a more detailed description of the units shown in Figs. 3 and 4. The section is separated into five units of similar thickness (in E–W direction; Fig. 2). A Massenkalk facies represents the beginning of the section (to the east; Figs. 3A–B, 4), followed by the fault zone which contains the highest amount of Variscan dolostones and calcites (Figs. 3D, 4). Towards the western side of the stratigraphic section, nearly equal amounts of Massenkalk and Variscan dolostones occur, followed by another unit dominated by the Massenkalk. The final unit (to the west) within the section is dominated by Variscan dolostone (Figs. 3D, 4).

**Table 1:** Description of the depositional and diagenetic facies in the Steltenberg quarry – Schwelm, Dorp fore-reef, and hydrothermal dolostone. Depositional facies according to [Krebs \(1974\)](#), and rock types after [Dunham \(1962\)](#). Thin section images are 5 cm in width.

Facies	Schwelm: bank/platform	Dorp: fore-reef	Hydrothermal dolostone
Rock type	Peloid-grainstone	Grain- to framestone	Crystalline
Rock matrix	Micritic	Mostly sparry matrix	Dolomitic matrix
Staining & mineralogy	Calcite >> Dolomite	Calcite	Dolomite > Calcite
Porosity	Very low; fracture-related	Low; fenestral, interparticle and microporosity	Medium; mostly fenestral, vuggy and intercrystalline
Allochem content	Calcspheres, peloids, thin-shelled bivalves, <i>Amphipora</i> -stromatopores	Tabular stromatopores, crinoids, brachiopods, rugose and tabular corals	No recognisable fossil content
Other features	Stylolites; recrystallised <i>Amphipora</i>	Fracture-bound calcite cementation; poorly sorted	Calcite veins and voids replace dolomite → dedolomitization
Stained thin section image			



**Fig. 2:** (A) East-west view into the Steltenberg quarry. (B) Dominant facies types of the stratigraphic section with estimated volume fractions of contributing phases. White numbers correspond to the present soles. The extent of the stratigraphic section shown in Fig. 4 is highlighted with a red line.

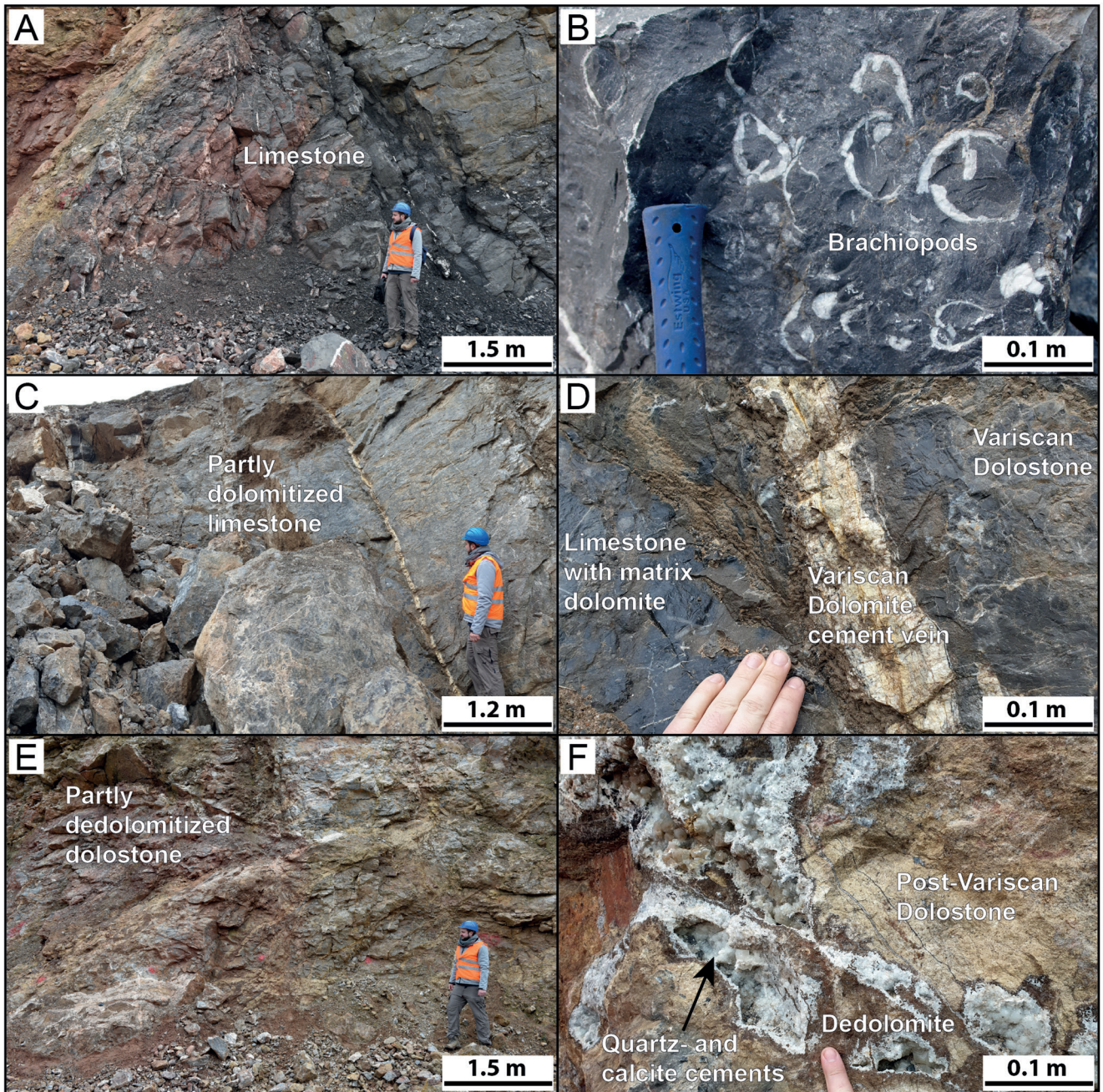


**Fig. 3:** Field images of the main facies types in the Steltenberg quarry. (A, B) Devonian Massenkalk limestone. (C, D) Partly dolomitised limestones and Variscan dolostones including dolomite cement veins. (E, F) Fault zone core including very porous post-Variscan dolomite-, dedolomite- and calcite cements.

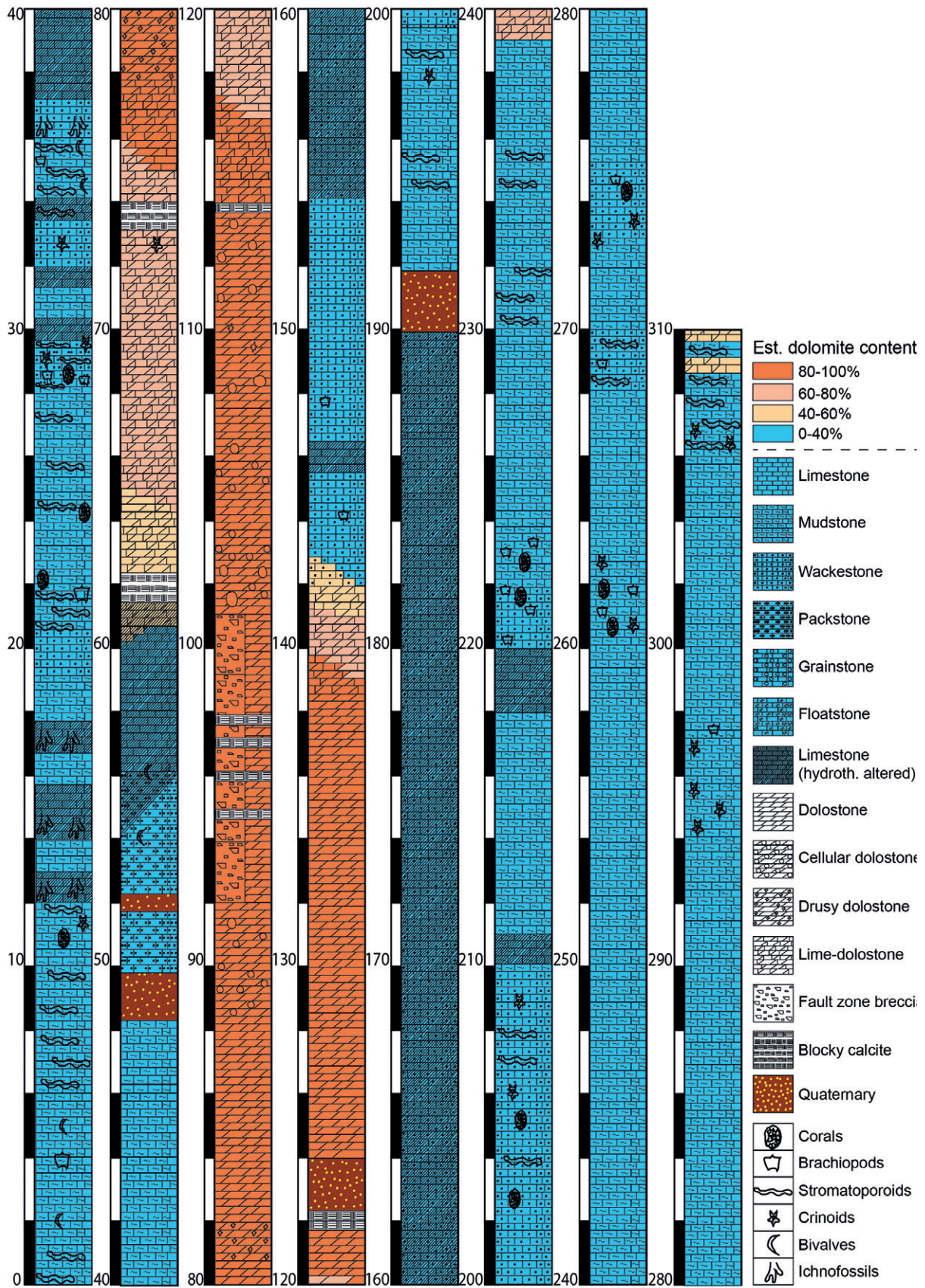


**Fig. 4:** Stratigraphic column of the measured section (0–310 m). Colour coding is based on estimated dolomite content from field and thin section observations.

## 4.2 Fault zone analysis and connectivity

Mesoscale (outcrop scale) fault zones including several bed-perpendicular and sub-parallel faults (slip surfaces) cut through the Steltenberg quarry's outcrops. The shear displacement was observed from the offset of bed boundaries and/or slip indicators (e.g. slickensides). Fig. 5 illustrates two main fault networks with many geometrical and kinematic complexities including increasing fault width, numerous fault cores, and associated subsidiary structures. The subsidiary structures are open fractures and veins that are mostly perpendicular to bedding and bedding-parallel stylolites.

The first fault network comprises a set of large normal faults with NNW–SSE orientation, which dip approximately 60–75°, with a 20–50 m wide fault zone. This fault zone includes a wide (10–40 m) damage zone composed of intensely fractured rocks with numerous fault cores defined by highly strained fault rocks, including non-cohesive and cohesive crush breccia and cataclasites (Figs. 5A, B). The fault cores vary from 0.2–2 m in thickness and accommodate a few centimetres to tens-of-metre offset. In contrast, the second, minor fault has a low dip (ca. 20–35°), ENE–WSW orientation, is largely sub-horizontal, much narrower (average of 3 m, but locally reaching 5 m). This fault zone's outer margin has

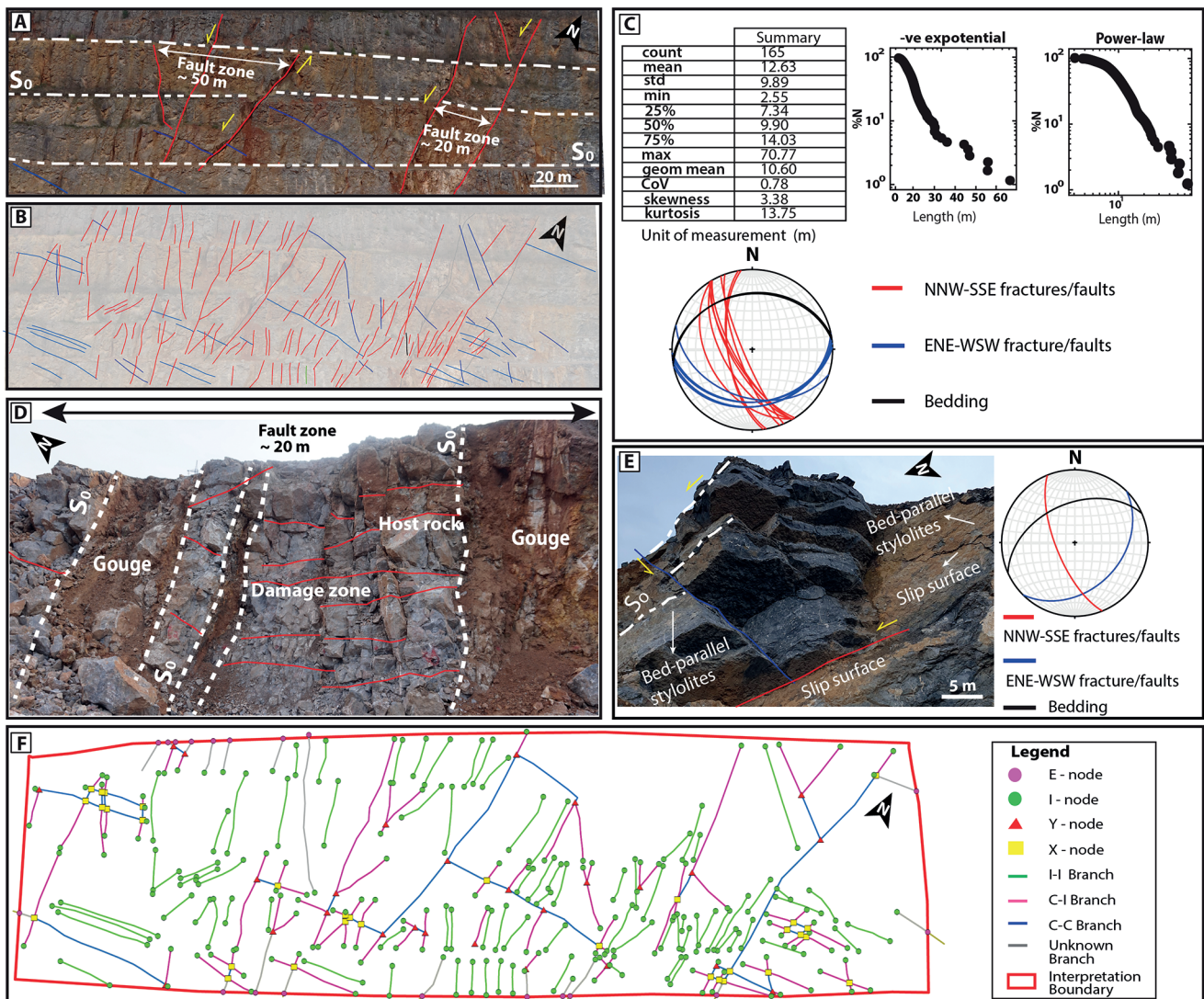


**Fig. 5:** Fracture/fault network architecture in the Steltenberg quarry. “ $S_0$ ” indicates bedding parallel. (A) High-resolution 2D outcrop orthorectified photograph showing the NE–SW view into the quarry with the dominant bedding perpendicular fault zones. (B) Map of digitised fracture/fault network patterns from the area shown in Fig. A; high angle NNW–SSE (red) and low angle ENE–WSW (blue). (C) Distribution analysis of fracture lengths from cumulative frequency plots and statistics from the digitised network of fractures/faults shown in Figs. A and B. The stereo plot shows the direction of the leading fracture/fault networks. (D) Field image (E–W view) of a typical bedding parallel fault zone with damage zones and fault cores, which cut bedding perpendicular open fractures. (E) Outcrop showing slip surfaces, bedding-parallel stylolites, and associated fractures. The stereo plot shows the fracture and bedding directions. (F) Topology of the fracture network shown in Figs. A–C classified into nodes and branches.

more resistant outcrops (in the narrow damage zone), while the inner core contains clay gouge, cohesive crush breccia and/or cataclasites (ca. 1 m thick), accommodating most of the local cumulative slip. Two similar striation sets were observed on these faults surfaces. One of the striations exhibits a horizontal movement in the same direction of the fault zone's hanging wall (approximately NNW–SSE). Conversely, the second set of striae lacks a visible sense of movement but generally trend N–S.

Overall, the number of the fault segments varies along the fault zones, exhibiting several connections due to differences in fault orientations (Fig. 5). Connections predomi-

nantly occur where two or more fault segments intersect, splay, cross-cut, or abut against another. A digitised fracture/fault network (Figs. 5B–F) suggests that both NNW–SSE and ENE–WSW fractures/faults are sub-parallel, pervasive, and regularly spaced (at 5–8 m and 3–5 m spacing, respectively). The cumulative length distribution has an average fracture/fault length of 12 m, fitting the negative exponential and power-law plots. These fracture/fault networks appear to have a moderate degree of connectivity based on their intersection (see Igbokwe et al. 2020 for a detailed description of topological analysis). Topologically, the abundance of isolated and splayed fault interactions linked with a high pro-

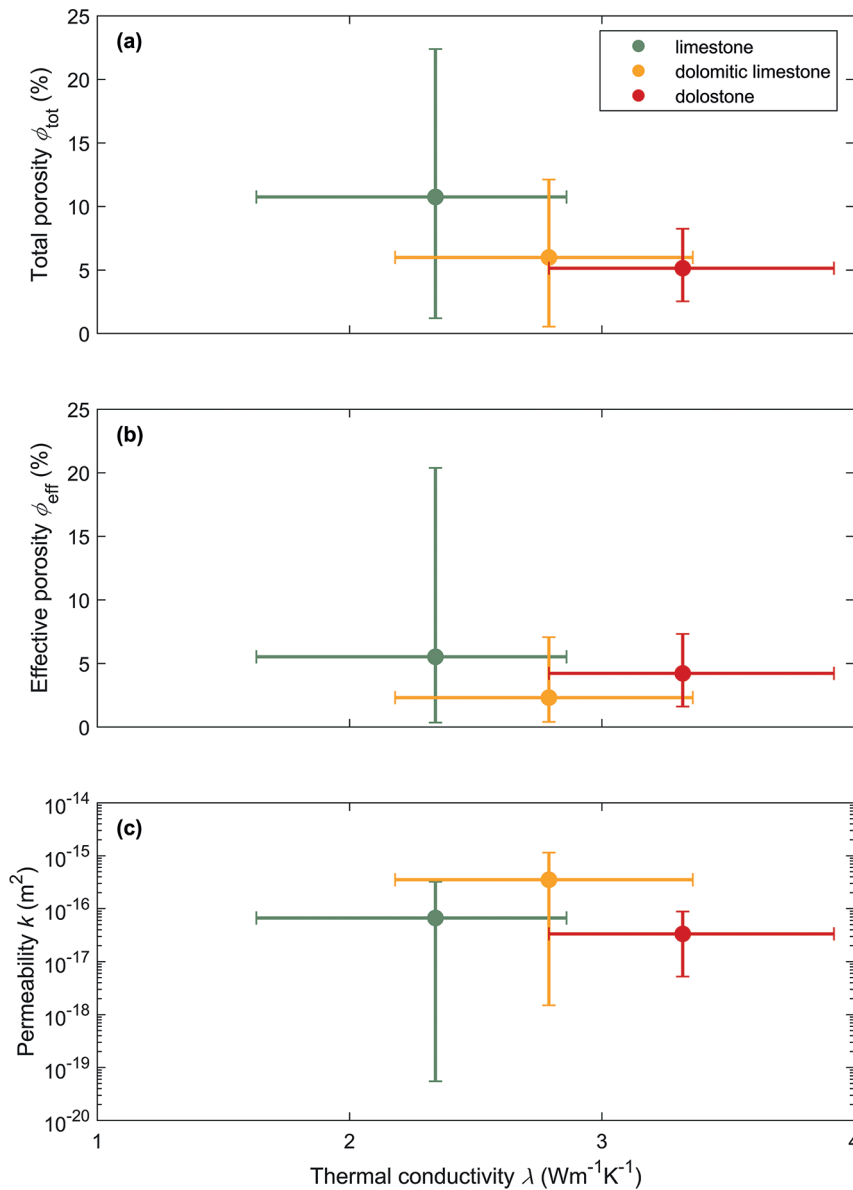


**Fig. 6:** Mean thermal conductivity ( $\lambda$ ) values of the Devonian carbonate samples from the Steltenberg quarry in Hagen plotted against the hydraulic properties represented by the mean values of the total porosity  $\phi_{\text{tot}}$  (a), the effective porosity  $\phi_{\text{eff}}$  (b) and the permeability  $k$  (c) for the three different mineralogical facies types. The lines crossing the mean data points represent the respective ranges from the minimum to the maximum values measured for every facies.

portion of I- and Y-nodes, and II or IC branches (Fig. 5F), while areas with dominant X-nodes and CC branches show higher fracture abundance and are linked to structurally complex zones.

### 4.3 Petrophysics

Effective and total porosity was determined for all 33 samples, while 32 were measured for thermal conductivity and 17 were measured for permeability (Fig. 6). The dolostone samples had the highest mean thermal conductivity values ( $3.32 \text{ Wm}^{-1}\text{K}^{-1}$ ) of all mineralogical facies types (limestone  $2.34 \text{ Wm}^{-1}\text{K}^{-1}$ ; dolomitic limestone  $2.79 \text{ Wm}^{-1}\text{K}^{-1}$ ), but the lowest mean total porosity (5.1%) and permeability ( $3.35 \times 10^{-17} \text{ m}^2$ ). The examined limestone samples had the highest mean total (10.8%) and effective (5.5%) porosity, while the dolomitic limestone samples had the highest mean permeability ( $3.51 \times 10^{-16} \text{ m}^2$ ). The standard deviation of all datasets (Fig. 6, supplementary tables) – especially the hydraulic properties – is the lowest for the dolostones, followed by the dolomitic limestones, while large deviations were observed for the limestone samples. The recognition of this large deviation is essential for the evaluation of reservoir potential of the limestone facies, especially as the minimum permeability of the limestone facies type is over three orders of magnitude lower than the mean, while the permeability of the dolostones only ranges from  $5.23 \times 10^{-18}$  to  $8.86 \times 10^{-17} \text{ m}^2$ . The standard deviation in thermal conductivity values are fairly similar for all facies types (Fig. 6, supplementary tables).

### 4.4 Petrology and geochemistry

#### 4.4.1 Cement stratigraphy

A paragenetic succession of the carbonates in the Steltenberg quarry was established from field observations (Fig. 3), thin section data, and cathodoluminescence analysis (Fig. 7). Dolomite terminology used here follows [Sibley & Gregg \(1987\)](#). The limestone (Massenkalk) precursor is characterised by fine- to medium-grained depositional facies, which include fossil brachiopods (*Stringocephalus burtini*), sponges, corals, bivalves, and crinoids. This phase generally has red luminescence (Figs. 7A, B). Occasionally, medium- to coarse crystalline dolomite rhombs occur in the rock matrix. The precursor limestone was partially or fully replaced by five dolomite cements and several hydrothermal and meteoric calcite cements. Dol 1 consists of fine to medium planar-s dolomite with patchy red luminescence (Figs. 7C, D). Dol 2 is divided into a fine- to medium-crystalline planar-s to nonplanar matrix dolomite (Dol 2A) and a nonplanar coarse-crystalline saddle dolomite (Dol 2B) with sweeping extinction and red-orange patchy luminescence (Figs. 7C, D). Dol 3 contains a medium- to coarse-crystalline planar-s dolomite (Dol 3A) and a coarse-crystalline saddle dolomite (Dol 3B) characterised by dark to bright red patchy luminescence (Figs. 7E, F).

Dol 3 is often overgrown by fine- to coarse-crystalline quartz phases (Qz 1 and Qz 2) with pale green to dark blue luminescence (Figs. 7E, F). Hydrothermal and meteoric calcites often fill open pores between dolomite grains or vugs, and overprint each other. These cements are characterised by dark red to yellow luminescence (Figs. 7G, H). Calcite cementation (LMC1 to LMC 4) is often associated with dedolomitisation (Dedol 1 and Dedol 2) of former dolomite phases (Figs. 7E, F). Stylolites are a product of pressure solution and often occur in the precursor limestone and Dol 1 to Dol 2 phases.

#### 4.4.2 Bulk geochemistry

The samples from the stratigraphic section bulk matrix display a large range in mineralogy, elemental concentration, and isotopic values (Table 2). Based primarily on field and laboratory estimates, mineralogy ranged from ca. 20–70% dolomite, with higher dolomite fractions located near the fault zone (Figs. 2–4). Elemental concentrations ( $n = 30$ ) vary correspondingly based on mineralogy and location relative to the fault zone. Ca concentrations range from 106,800–405,570 ppm (average = 273,848 ppm), Mg concentrations vary from 734–125,200 ppm (average = 40,395 ppm), Sr concentrations from 13–1,032 ppm (average = 243 ppm), Fe concentrations from 97–19,060 ppm (average = 4831 ppm), and Mn concentrations range from 124–3800 ppm (average = 895 ppm) (Table 2). In general, as Ca concentrations decrease, Mg and/or Fe concentrations increase.  $\delta^{13}\text{C}$  and  $\delta^{18}\text{O}$  values also vary greatly throughout the stratigraphic section, with  $\delta^{13}\text{C}$  values ranging from -7.3 to 4.6‰, and  $\delta^{18}\text{O}$  values varying from -11.3 to -7.1‰ (Table 2). The lowest  $\delta^{18}\text{O}$  values occur towards the end of the section around 280 m, and the highest values occurring at 180 m. For clarity, the geochemical data plot into three main clusters with regard to the measured section: (i) the easternmost unit dominated by Massenkalk facies (0–75 m), (ii) the fault zone unit in the centre of the section (75–175 m), and the Variscan dolomite unit towards the westernmost point (175–320 m). The fault zone unit is characterised by the lowest  $\delta^{13}\text{C}$  values (average = 0.5‰), highest  $\delta^{18}\text{O}$  values (average = -6‰), the highest Mg and Mn concentrations (average = 56,470 and 1,559 ppm, respectively), and the lowest Sr concentrations (average = 149 ppm) (Table 2). Strontium ratios show great variation between the three major stratigraphic units. The Massenkalk unit at the beginning of the section (measured at 0 m) has a  $^{87}\text{Sr}/^{86}\text{Sr}$  ratio of 0.707962, the fault zone (measured at 140 m) has the highest ratio at 0.710712, and the Variscan unit towards the end of the section has a ratio of 0.707988 (Fig. 8).

#### 4.4.3 Phase-specific cement geochemistry

The limestone precursor (MK) bulk matrix contains up to 30% quartz and up to 20% dolomite, while all dolomite phases contain traces of calcite (Table 2). Phases Dol 1 and Dol 3A are iron-rich and may contain traces of ankerite. The calcite cements are primarily low in Mg concentrations, with

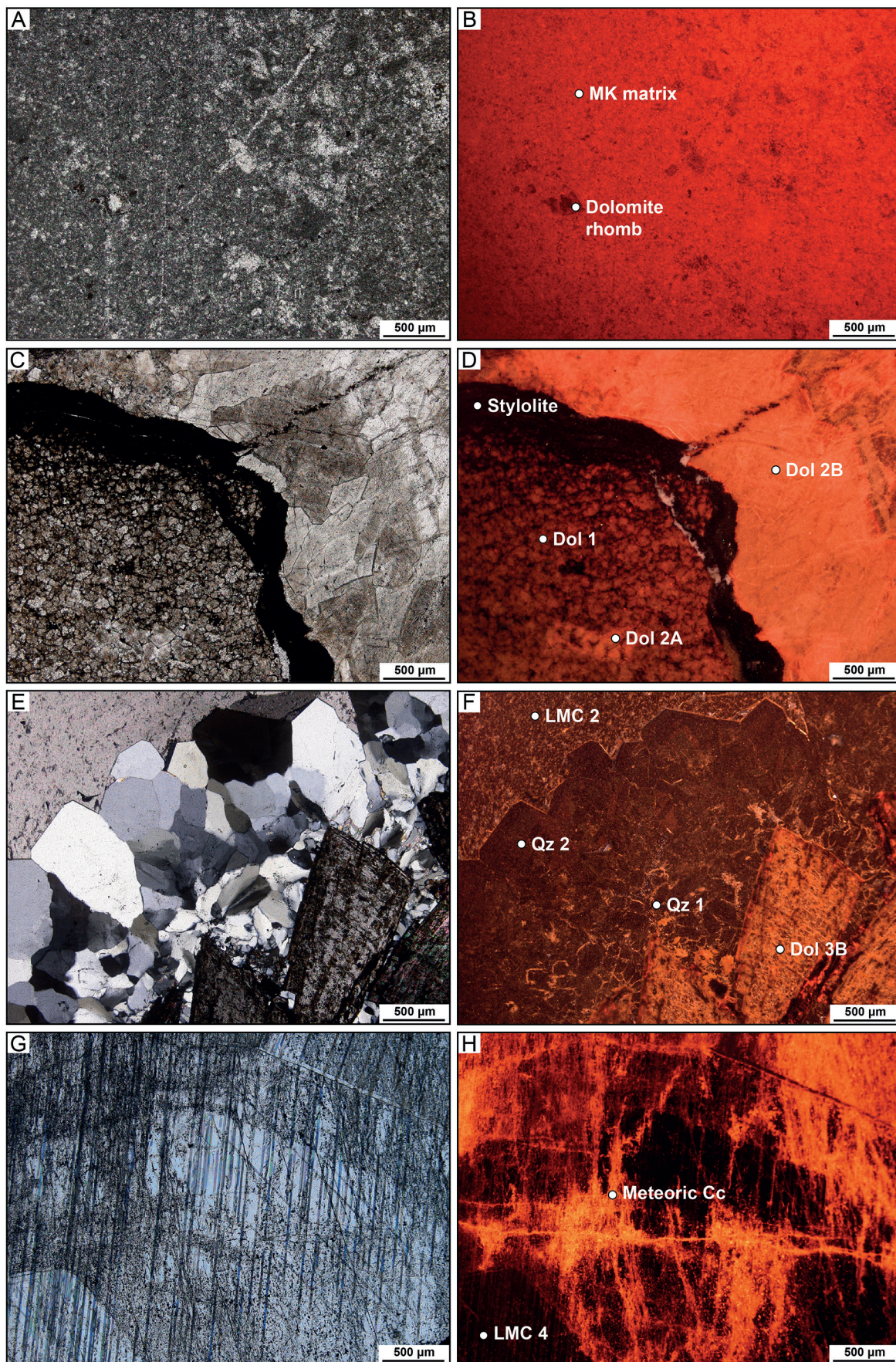


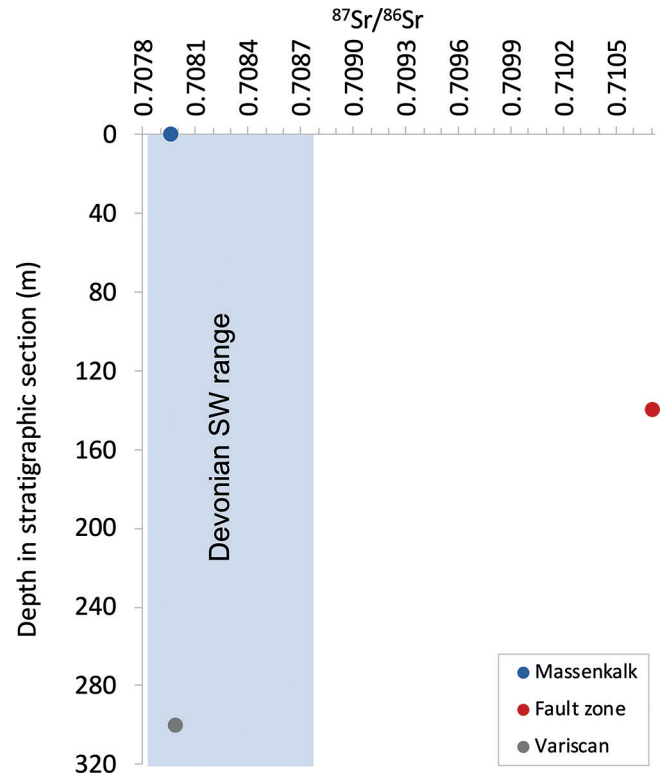
**Fig. 7:** Transmitted light and corresponding cathodoluminescence images of the carbonates in the Steltenberg quarry. (A, B) Massenkalk limestone including few dolomite rhombs grown in the matrix. (C, D) Variscan dolomites Dol 1, Dol 2A and Dol 2B. Note the stylolite that developed during pressure solution. (E, F) Post-Variscan phases from the fault zone core including the typical post-Variscan paragenesis from dolomite precipitation to quartz and later hydrothermal calcite cements. (G, H) Hydrothermal calcite cements, which show typical features of later overprint by meteoric calcites precipitating from microfractures and along cleavage planes.

**Table 2:** Geochemistry results of all samples including the stratigraphic section (“section”) and cement specific phases (“cement”). All values are reported as averages for each sample group. See supplementary tables for all corresponding data and standard deviations.

Sample type	Facies/Cement type	$\delta^{13}\text{C}$ av. (‰ VPDB)	$\delta^{18}\text{O}$ av. (‰ VPDB)	Ca av. (ppm)	Mg av. (ppm)	Sr av. (ppm)	Fe av. (ppm)	Mn av. (ppm)
Section	All samples	1.9	-7.1	273,848	40,395	243	4,831	895
Section	Massenkalk (n = 7)	1.8	-7.0	315,669	5,516	363	3,278	389
Section	Fault Zone (n = 10)	0.5	-6.0	268,589	56,470	149	3,463	1,559
Section	Variscan (n = 13)	3.0	-8.0	255,375	46,811	250	6,720	657
Cement	Massenkalk matrix (n = 6)	2.9	-6.0	336,152	6,632	568	4,499	159
Cement	Dol 1 (n = 6)	3.3	-9.1	219,902	125,183	31	509	943
Cement	Dol 2A (n = 6)	3.2	-7.5	245,090	105,712	57	5,020	1,720
Cement	Dol 2B (n = 3)	3.2	-9.3	224,167	123,300	41	721	625
Cement	Dedol 1 (n = 3)	-1.8	-6.2	300,673	67,137	33	2,249	1,993
Cement	Dol 3A (n = 3)	3.1	-7.0	216,530	110,500	24	7,968	2,123
Cement	Dol 3B (n = 5)	0.4	-4.6	225,904	114,176	20	6,750	2,876
Cement	Dedol 2 (n = 6)	-5.1	-5.8	360,828	11,487	36	2,710	2,067
Cement	LMC 2 (n = 3)	1.0	-6.0	397,373	988	97	1,708	1,497
Cement	LMC 3 (n = 8)	1.8	-11.3	396,243	2,534	215	312	450
Cement	LMC 4 (n = 6)	0.4	-6.5	392,093	2,601	193	1,795	2,230

low amounts of Mg-calcite also present. Average carbon ( $\delta^{13}\text{C}$ ) and oxygen ( $\delta^{18}\text{O}$ ) isotope values of all paragenetic phases are shown in Table 2. The limestone precursor matrix has average  $\delta^{13}\text{C}$  and  $\delta^{18}\text{O}$  values of 2.9‰ and -6.0‰ (n = 6), respectively. Dol 1 has an average  $\delta^{13}\text{C}$  value of 3.3‰ and  $\delta^{18}\text{O}$  value of -9.1‰ (n = 6). Dol 2A has average  $\delta^{13}\text{C}$  and  $\delta^{18}\text{O}$  values of 3.2‰ and -7.5‰ (n = 6), respectively. Dol 2B has an average  $\delta^{13}\text{C}$  value of 3.2‰ and  $\delta^{18}\text{O}$  value of -9.3‰ (n = 3). Dedol 1 has average  $\delta^{13}\text{C}$  and  $\delta^{18}\text{O}$  values of -1.8‰ and -6.2‰ (n = 3), respectively. Dol 3A has an average  $\delta^{13}\text{C}$  value of 3.1‰ and  $\delta^{18}\text{O}$  value of -7.0‰ (n = 3). Dol 3B has average  $\delta^{13}\text{C}$  and  $\delta^{18}\text{O}$  values of 0.4‰ and -4.6‰ (n = 5), respectively. Dedol 2 has an average  $\delta^{13}\text{C}$  value of -5.1‰ and  $\delta^{18}\text{O}$  of -5.8‰ (n = 6). LMC 2 has an average  $\delta^{13}\text{C}$  of 1.0‰ and  $\delta^{18}\text{O}$  value of -6.0‰ (n = 3). LMC 3 has an average  $\delta^{13}\text{C}$  of 1.8‰ and  $\delta^{18}\text{O}$  of -11.3‰ (n = 8). LMC 4 has an average  $\delta^{13}\text{C}$  of 0.4‰ and  $\delta^{18}\text{O}$  of -6.5‰ (n = 6).

**Fig. 8:** Strontium ratios for the three measured units within the stratigraphic section. Depths correspond to the E–W trending stratigraphic section shown in Fig. 2. The blue rectangle indicates the range of depositional  $^{87}\text{Sr}/^{86}\text{Sr}$  values of seawater (SW) during the Devonian as indicated by Howarth & McArthur (1997).



## 5. Interpretation and discussion

### 5.1 Depositional model and facies types

The large-scale platform and basin architecture of the Devonian carbonates in the subsurface of NRW is poorly understood, with the majority of evidence coming from outcrops and their correlation. Ongoing work will provide a refined degree of knowledge by means of cores and seismic lines. The findings presented here reveal the shedding of reefal material derived from the Devonian bioherms near Hagen (Krebs 1974), to the west of the study area. A compilation of these two aspects and their effects in the Steltenberg quarry is displayed in Fig. 9A. The mostly siliciclastic top and foot-wall layers of the Flinz shales and limestones, and the Upper Honsel Beds respectively, framing the Schwelm and fore-reefal subtype of the Dorp Facies, do not actually crop out in the quarry. According to Krebs (1974), the dark-bituminous Flinz shales form the inter-reef basins in regions where the reefal buildups of the Dorp Facies is not developed. Furthermore, Krebs (1974) stated that one of the largest reefal bioherms of the Devonian carbonate complex along the northern flank of the Remscheid-Altena Anticline is located 10–12 km west of the study area, while a smaller reefal buildup of the Dorp Facies is located to the west of the Steltenberg quarry (Fig. 9B). We argue that the core of this minor reefal body is not cropping out in the quarry itself. Our argument is that evidence for massive coral-stromatoporoid framestone or bafflestone units, fringed by reefal debris are not present. Having said that, we do not exclude the possibility that localised metre-scale patch reefs in a lagoonal setting existed at some stage. Where this was the case, these small bioherms were prone to storm-wave disintegration resulting in fragmentation and transport of the reefal components.

Because the coastline of the Old Red continent was located to the northwest (Grabert 1998), and the regionally important reefal bodies were situated to the west of the study area, the occurrence of fore reef lithologies of the Dorp Facies in the Steltenberg quarry is easily explained. The Devonian carbonate complexes on the northern flank of the Remscheid-Altena Anticline arguably formed isolated patches of barrier reef bodies on the outer shelf, rather than a coherent fringing reef shielding off a lagoonal and a protected back reef environment. The Devonian reefal systems are not easily separated into fore-reef, main reefal body and back-reef environments. Hence, we propose that the well-defined fore-reef facies, as exposed in the Steltenberg quarry (Krebs 1974) is not necessarily a template for other locations situated at similar distances/orientation to the main reefal belts. No detailed allocation of the reefal debris contained in outcrops and in thin sections of the fore-reef facies to one of the two potential reefs west of the study area has been performed, if at all possible. The assumption, however, that the availability of this facies type decreases towards the east (Fig. 9A) is highly likely due to the position of the reef bodies (Fig. 9B).

According to Krebs (1974), the Schwelm Facies is stratigraphically the lowermost succession of the Devonian car-

bonates in the study area. Hence, its location in the Steltenberg quarry and its position in Fig. 9A is coherent. In contrast, better understanding the exact local depo-facies geometry within the quarry is a work in progress. Problems occur due to widespread fabric-destructive dolomitisation of the precursor facies, which hinders the assignment of rock types and biota to specific environments and provenance. The Iberg Facies is absent in the study area, which can be explained by its generally stratigraphically patchy occurrence and the lack of exposures of the Dorp Facies reef-core in the quarry (Krebs 1974). The facies type colour code in Fig. 9A documents the distribution and relative volumetric significance of the various facies types and carbonate mineralogies throughout the Steltenberg quarry.

In summary, given the regionally limited outcrop data at hand, the interpretation of the depositional environment in the Steltenberg quarry is not trivial. Moreover, the Devonian reefal complex formed during a period in Earth's history that facilitated reef growth even in depositional areas that are otherwise hostile (sediment-stressed) to reefal organisms. The largest regional reefal bioherms of the Devonian carbonate complex are located 10–12 km west of the study area and outcrops in the Steltenberg quarry likely reveal a complex interplay of reefal debris transported by currents and waves and localised patch reefs that were prone to wave disintegration. Different facies types adds to the regional complexity. Fabric-destructive dolomitisation of the precursor facies often limits the assignment of rock types and biota to specific environments and provenance.

### 5.2 Palaeo-fluid flow related to a regional fault zone

The three-dimensional porous media fluid flow (and heat transfer) in geothermal reservoirs, and the volume of the fluid migration averaged over time, are the most significant parameters in geothermal reservoir characterisation (Mueller et al. 2010; Hu et al. 2013; Balcewicz et al. 2021). We argue that in order to understand these parameters, the diagenetic pathways and the palaeo-fluid flow in a given reservoir unit are of great significance. This is because next to fracture-related flow, facies spatial distribution and the formation and destruction of porosity and permeability in carbonates, affect these parameters. These patterns in turn, are directly linked to the diagenetic reactivity of carbonates throughout their burial and the nature and volume of corrosive or oversaturated fluids the carbonates encounter in the subsurface. Evidence for palaeo-fluid flow is recorded in the paragenetic succession of various carbonate cements as present in the fault zones studied here. The paragenetic succession of the carbonates in the Steltenberg quarry is complex, with cement petrography (Fig. 10) and phase specific geochemistry (Fig. 11) being closely linked to processes which generate and reduce porosity.

The history of the studied Devonian carbonates commences with the deposition of Givetian-Frasnian (388 to 372 Ma) shallow marine reefal deposits. During early marine

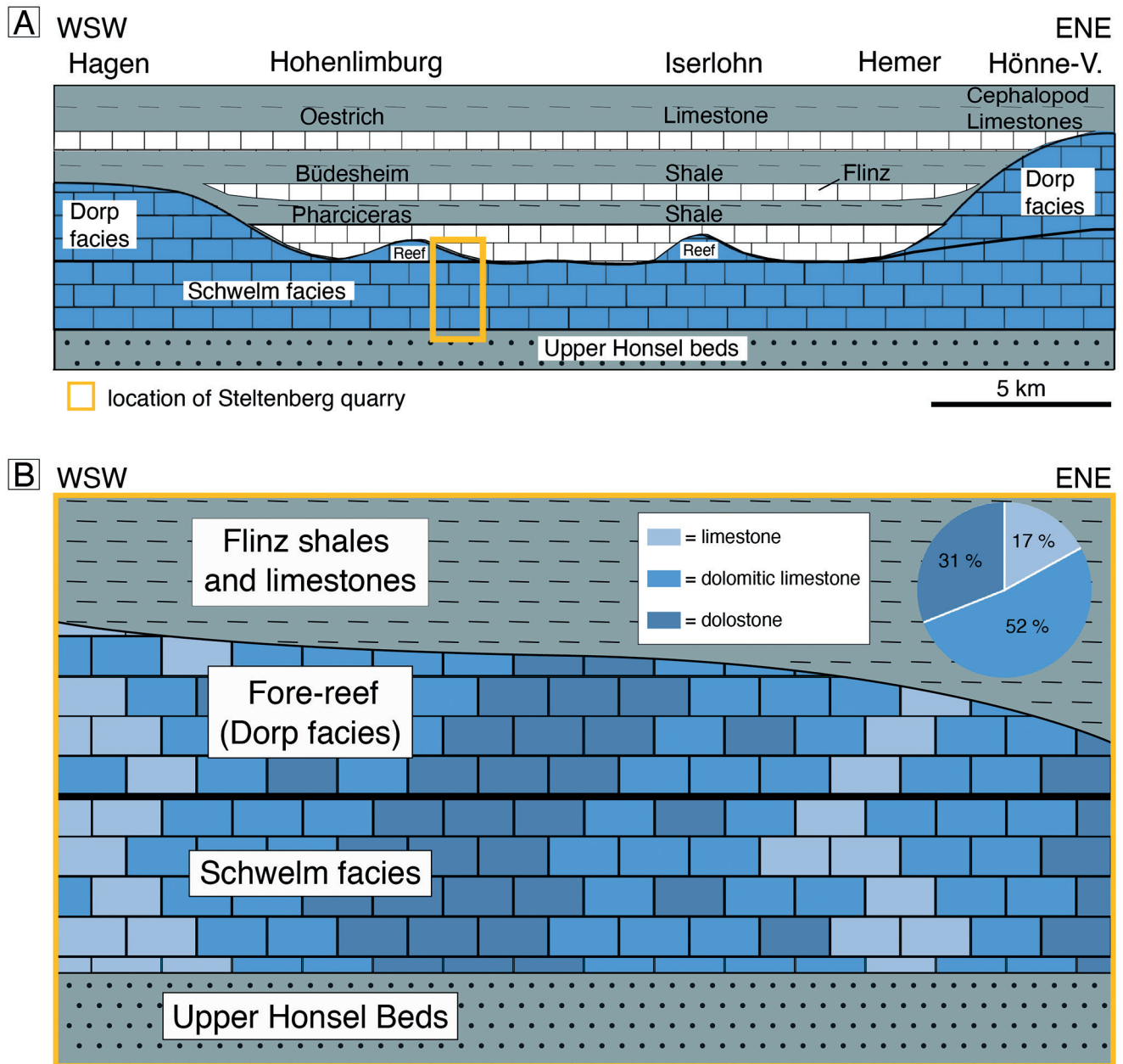


**Fig. 9:** (A) Cross-sectional schematic redrafted from Krebs (1974) through the carbonate range on the northern flank of the Remscheid-Altena Anticline from Hagen to Hemer (after Beckmann 1948; Rosenfeld 1961; Kamp 1968; Krebs 1974). The yellow frame marks the location of the Steltenberg quarry, which is schematically displayed in (A). (B) Depositional and mineralogical facies model of the Devonian carbonate depositions of the Steltenberg quarry in Hagen including top and footwall layers of siliciclastic sediments: the limestone-bearing Flinz shales and the Upper Honsel Beds mostly made up of fine-grained sandstone (Krebs 1974; Koch et al. 2018). The carbonates, displayed as a tiled pattern, are represented by the Schwelm Facies and the fore-reef subtype of the Dorp Facies and are equally affected by the fracture-related, hydrothermal dolomitisation leading to the quarry-wide mineralogical facies distribution as indicated by the colouration of the tiles and shown in the cake diagram.

diagenesis of the Massenkalk precursor sediments (MK; Figs. 7A, B), a first stage of cementation and low-grade porosity reduction was marked by precipitation of marine cements and recrystallisation of aragonitic shells (Götte 2004). During subsequent shallow- to deep-burial diagenesis in the Devonian and Carboniferous, extensive cementation and compaction significantly reduced the porosity and permeability

of these limestones (Fig. 10). Most precursor units record marine Givetian-Frasnian carbon-isotope values ( $\delta^{13}\text{C}$ ) between 2.5 and 3.0‰. The trend toward lighter  $\delta^{18}\text{O}$  values from -5 to -7‰ may indicate warm burial fluids (Fig. 11). This interpretation is supported by dark-red to bright-orange luminescence colours, typical for the burial diagenetic regime (Bruckschen & Richter 1993). The process of porosity

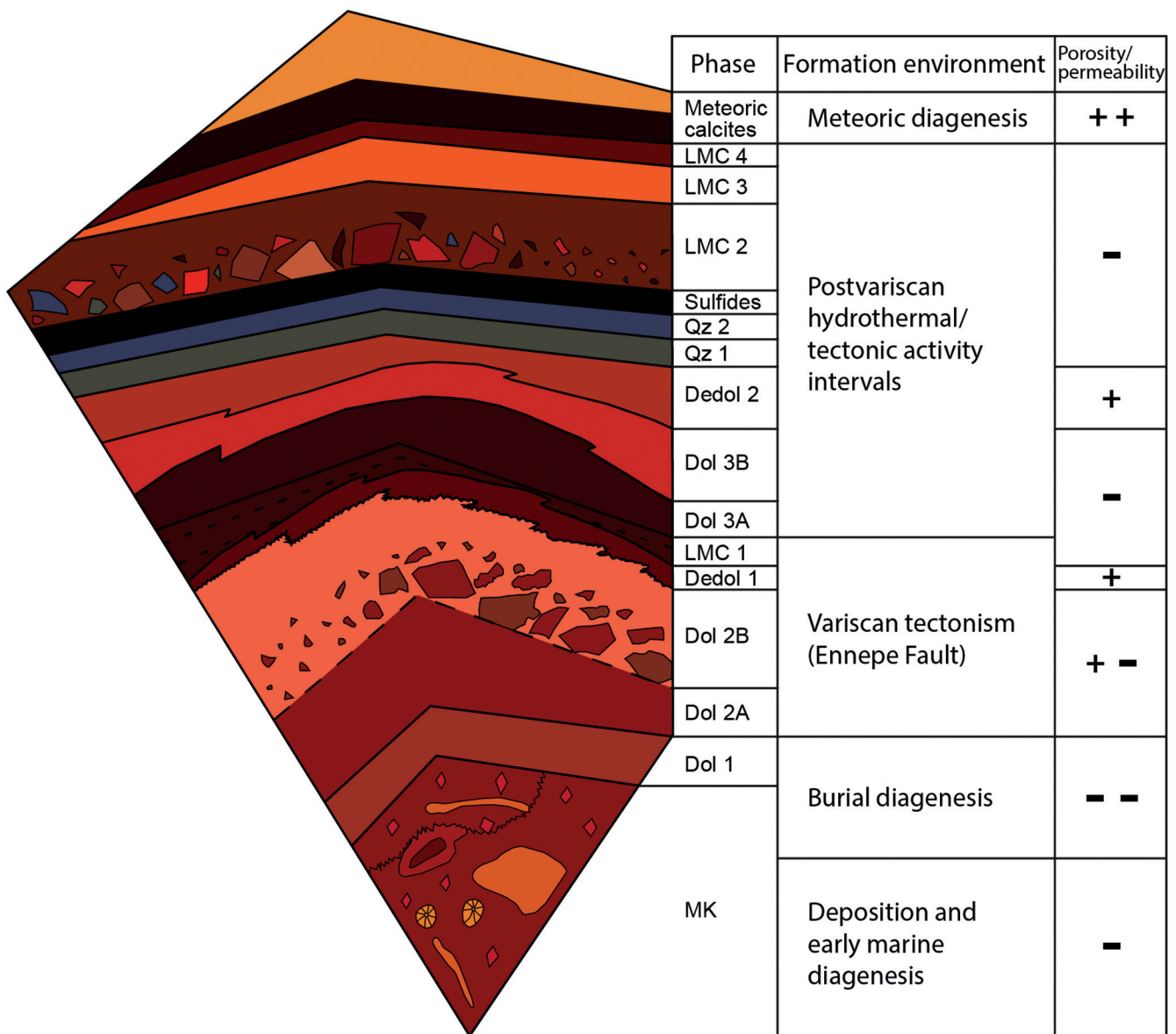


**Fig. 10:** Complete paragenesis of diagenetic phases in the Steltenberg quarry with typical cathodoluminescence colours related to their diagenetic and tectonic environment of precipitation or formation. Porosity and permeability reducing phases are marked with a “-“. Porosity and permeability generating phases are marked with a “+“. Tectonic activity phases and formation environments were compiled after [Götte \(2004\)](#) and references therein.

reduction was completed when the replacement dolostone (Dol 1) formed. Dol 1 is generally abundant along bedding planes and was previously interpreted as burial dolomite that may also be related to tectonism in an early stage of the Variscan Orogeny ([Gillhaus et al. 2003](#)). A burial diagenetic origin is further suggested by low  $\delta^{18}\text{O}$  values (down to -9‰) of this cement phase.

During the course of peak tectonic activity during the Variscan Orogeny (Late Carboniferous), hydrothermal fluids traversed through and reactivated older, early stage Variscan faults. One of these faults is the Ennepe Thrust, which is partly exposed in the Steltenberg quarry ([Thome 1970](#); [Drozdowski & Wrede 1994](#)). The dolomite phases

Dol 2A and Dol 2B (Fig. 7C, D) are abundant along fractures following the main strike-direction of the Ennepe Thrust. While Dol 2A exclusively occurs as matrix dolomite in former precursor limestones, Dol 2B generally forms as void-filling saddle dolomite cement around breccia clasts in decimetre-sized fractures and in millimetre- to centimetre-sized fractures in precursor limestones. Saddle dolomite is characterised by curved crystal faces and sweeping extinction ([Radke & Mathis 1980](#)), and indicates fluid temperatures above 80 °C ([Mueller et al. 2020](#); [Davies & Smith 2006](#)). Both dolomite phases were previously interpreted to have one contemporaneous formation mechanism ([Gillhaus et al. 2003](#)). However, their oxygen isotope

values differ by up to 2.5‰ (Fig. 11), suggesting different precipitation pathways.

Due to the fracture-bound nature of these two dolomites and the already very low porosity of precursor phases, the bulk rock porosity did not significantly change. This diagenetic stage was followed by the precipitation of LMC 1 in some locations (Fig. 10). Dedol 1 marks a shift in fluid chemistry from Mg-saturated fluid to undersaturated conditions (with respect to carbonate minerals) following Late Variscan hydrothermal activity. Götte (2004) interpreted this phase (and subsequent stages of dedolomitisation) as alteration phases of instable hydrothermal minerals, karstification and neomorphism in the meteoric realm. This interpretation is strengthened by low carbon-isotope values (down to -3.5‰) in Dedol 1 (Fig. 11). Dissolution of cement phases also resulted in increased porosity and permeability (Fig. 10).

After a precipitation hiatus in the order of tens-of-millions-of-years, the rocks in the Steltenberg quarry were influenced by several intervals of post-Variscan hydrothermal activity, potentially tectonically-triggered (Drozdowski & Wrede 1994; Gillhaus et al. 2003; Götte 2004). The first Mesozoic, and arguably the most influential of these intervals, was driven by over-pressured hydrothermal fluids, which migrated along the NNW–SSE striking faults. Their cement precipitates dominate portions of the Steltenberg quarry (Fig. 2). The formation of the most volumetrically significant Dol 3A and Dol 3B phase led to a general decrease in porosity. These fabrics are saddle dolomites precipitated at elevated temperatures (Fig. 10). Geochemically, Dol 3A is very similar to the precursor limestone and Dol 2A, with nearly identical  $\delta^{18}\text{O}$  values (Fig. 11). Gillhaus et al. (2003) recognised growth of Dol 3A on top of Variscan dolomite phases, which may point to a spatially close inter-growth of dolomite phases that are difficult to isolate and analyse. In contrast, Dol 3B from the core of the post-Variscan mineralisations (Figs. 7E, F) is geochemically distinct from Dol 3A. Carbon-isotope values of Dol 3B are 3‰ lower compared to Dol 3A, while  $\delta^{18}\text{O}$  values are up to 4‰ higher (Fig. 11). A change in fluid composition resulted in two stages of quartz cementation. Sulphides precipitated locally in open vugs (Figs. 7F, 10).

For geothermal reservoir potential, the second phase of dedolomitisation and karstification merit attention. All carbonates along the NNW–SSE striking fault system were affected by intense dedolomitisation and in part brecciation. This resulted in reactivation of pathways for fluid circulation and a significant increase in bulk-rock porosity and the opening of vugs up to several decimetres in diameter. Dedol 2 is characterised by even lower  $\delta^{13}\text{C}$  values compared to Dedol 1 (as low as -7.5‰; Fig. 11), indicating meteoric fluids may have interacted with oxidised organic matter in overlying soils (Swart 2015). Subsequent precipitation of post-Variscan hydrothermal calcite cements LMC 2, 3 and 4 suggest additional hydrothermal activity (Fig. 10). Cements LMC 2 and 4 yield similar oxygen isotope values as younger hydrothermal phases. Only LMC 3 is characterised by significantly more negative  $\delta^{18}\text{O}$  values compared to all other phases, indicating

a strong burial diagenetic influence (Fig. 11). Based on oxygen isotope thermometry, Götte (2004) proposed a fluid temperature between 100 and 140 °C.

Regional hydrothermal activity became less significant in the Palaeogene. The renewed influence of meteoric diagenesis resulted in corrosion of post-Variscan dolostones and the precipitation of volumetrically important calcite cements. As recognised in the Steltenberg quarry, this process along with the near-surface exposure of the carbonates led to large-scale karstification in this portion of NRW between the Oligocene and particularly the Quaternary (Hammerschmidt et al. 1995; Richter 1995). There is no indication that these later stage processes should be relevant for the analogous units in the subsurface.

In conclusion, a clear understanding of the diagenetic history of a given geothermal reservoir unit is a prerequisite for extrapolation between outcrop analogues and their corresponding subsurface units. The case example documented here clearly documents the complexity of the processes involved. Of particular interest are dissolution-reprecipitation processes and changes in carbonate mineralogy (such as limestone-dolostone recrystallisation) along burial pathways often controlled by tectonic processes. Next to burial hydrothermal dolomitisation (and dedolomitisation), meteoric karstification is of great relevance. Care must be taken, however, to separate between Holocene (post exhumation) karst features and ancient karstification. Whereas the most recent karstification as exposed in quarries has often limited significance for deep-seated carbonate rock bodies, a careful evaluation of cement fabrics and their mineralogical and geochemical properties has great potential to reveal evidence for ancient stages of karst formation that may have affected units prior to burial.

### 5.3 Effect of regionally-important fault zones and related hydrothermal dolomitisation on geothermal reservoir properties

Fault zones control the upper crust's mechanical and fluid-flow properties, where the semi-brittle shear zone or pre-existing or early formed brittle structures that locally perturb the stress state dominate the process of fault development (Davatzes et al. 2005; Davatzes & Aydin 2003; Faulkner et al. 2010). Recently, several studies of carbonate rocks have documented the control of fault activity by pre-existing anisotropies within the host rock, for example, bedding surfaces, veins, pressure solution seams and barren fractures (Agosta & Aydin 2006; Billi et al. 2003; Rustichelli et al. 2012 and references therein). Such anisotropies induce variations in the attitude of fault segments and fracturing mode. As fault zones grow, progressive shearing and interaction of the inherited structures lead to slip zones and slip surfaces – adapted in the fault cores and damage zones – and, in turn, affect the host rock properties. The degree to which the fault zone impacts the host rock properties is related to (i) the morphological position of the fault's internal structure components (i.e. core, damage zone or protolith), (ii) material

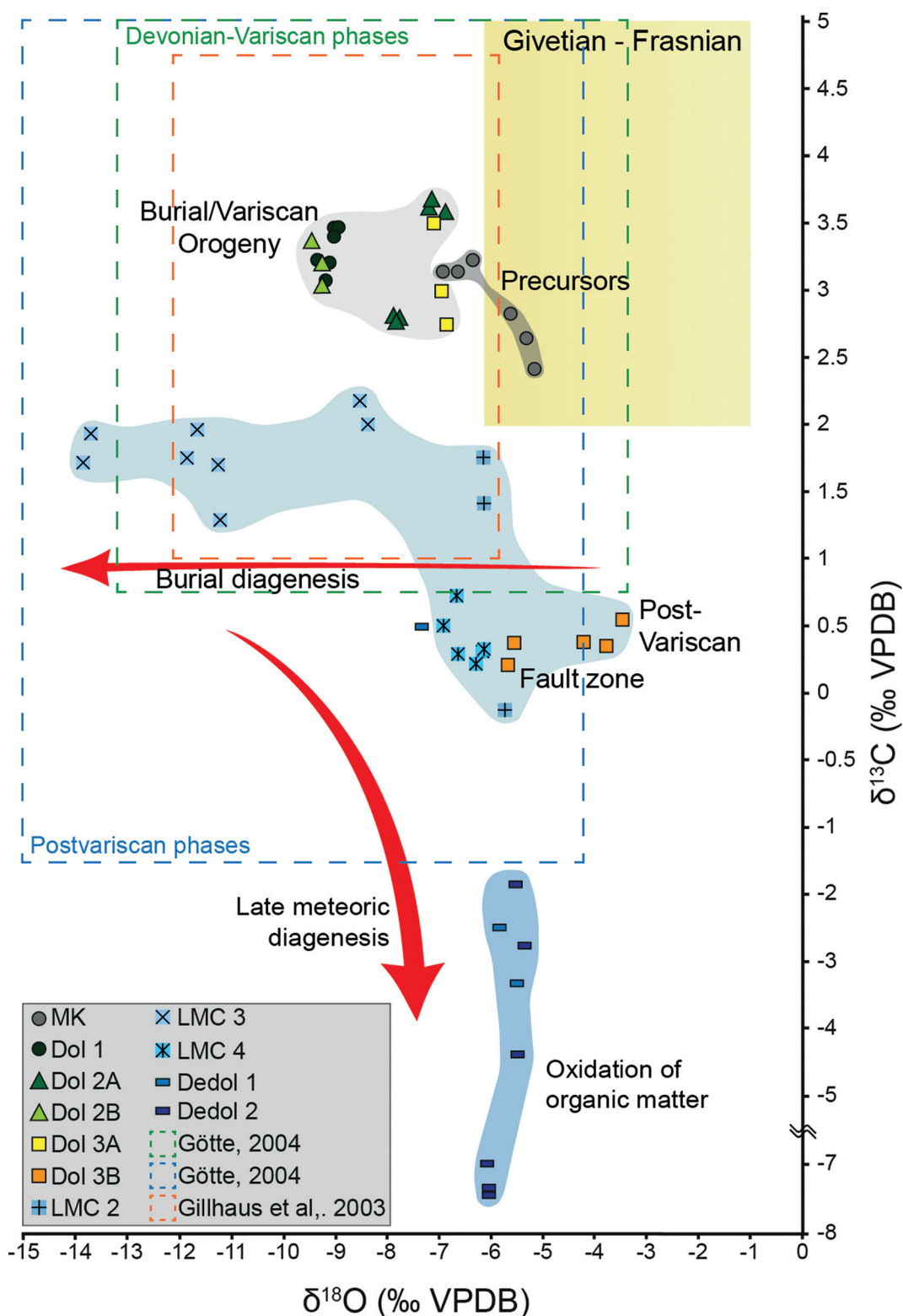


**Fig. 11:** Cross-plot of phase specific  $\delta^{18}\text{O}$  and  $\delta^{13}\text{C}$  data for all analysed samples of dolomite and calcite phases at Steltenberg quarry. The stable isotopic composition of Devonian (Givetian-Frasnian) marine calcites are indicated in the yellow and stippled purple boxes (from Grossman 2012; Saltzman & Thomas 2012; Veizer & Prokoph 2015). Two dominant trends are present: burial diagenesis led to lighter oxygen values (down to -14 ‰) and meteoric diagenesis to lighter carbon values (down to -7.5 ‰).

properties, and (iii) fault dimensions (Davatzes et al. 2005). The impact of the local fault systems, such as the WSW–ENE striking Ennepe Thrust (Variscan) and the NNW–SSE striking normal faults (post-Variscan Orogeny), on the distribution of dolostone and limestone in the study area (Gillhaus et al. 2003) is of general significance.

At Steltenberg quarry, the NNW–SSE and WSW–ENE oriented fault zones (Fig. 5) are composed of high-strain fault cores (approximately 0.2 to 5 metres in width) surrounded by a damage zone, ranging between 10 and 40 metres in width. In general, the damage zones in Steltenberg quarry are 5 to 10 times larger in width compared to the fault cores, which may play critical role in fluid flow (e.g. Faulkner et al. 2010). The width of the damage zone has been shown to positively correlate with the displacement magnitude of the fault, which was also observed in the Steltenberg quarry (Fig. 5A). The fault core comprising fault gouge, breccia and cataclasites accommodate most of the displacement. The slip zones cut the Devonian cataclasite dolostones, some of which are cement-supported. Clasts are sub-angular and fragmented by bulk extensional fracturing and comminution. Reduction in grain-size towards the slip surfaces leads to the formation of ultracataclasites. As documented here, the multitude of minor structural features in the damage zone, combined with the high porosity and permeability fault core, are genuine fluid “highways” that significantly affect reservoir properties. In case these fluids are oversaturated with respect to CaMg carbonate, pervasive replacement of precursor limestones by dolostones would result. Although the presence of cataclasites and ultracataclasites can suggest high anisotropic permeability, the volume of cataclastic rocks in the quarry is relatively low, especially from a regional context. Thus, it is assumed that the observed cataclasites will have little impact on the fluid movement.

Based on local bulk XRD-measurements and visual interpretation of carbonate mineralogy in the studied section in the quarry, the following relative percentages of carbonate mineralogies result: ca. 17% limestone, 52% partly dolomitised limestone and 31% dolostone, depending on the location within the quarry (Fig. 9). The quantitative evaluation will be studied in greater detail in forthcoming work by conducting bulk XRD-measurement along the measured stratigraphic section. Nevertheless, the data indicated here serves to contrast and compare the significance of carbonate mineralogies along the northern flank of the Remscheid-Altena Anticline. For instance, the present data suggest considerably higher amounts of dolostone and dolomitic limestone in Hagen compared to quarries in Wuppertal and in the Hönne Valley. This has implications for geothermal reservoirs as dolomitised (and dedolomitised) carbonate lithologies have significant potential. However, the data shown here also document the difficulty of simplistic correlations of data from one location to the subsurface. Moreover, our data reveal a rather complex suite of different dolomite types that represent different formation stages.

The local predominance of the dolostone along the central part of the section in Figs. 2B and 9 is in good agreement with the hydrothermal, fracture-related origin of dolomitising

fluids (Gillhaus et al. 2003; Götte 2004). Moreover, the common occurrence of saddle dolomite cements in that area is also in agreement with hydrothermal fluids. We argue that in contrast to diffuse regional bulk-rock dolomitisation, spatially well-constrained hydrothermal dolomitisation is most pronounced along regional fault systems, such as the case of the Ennepe Thrust. Given the significance of the NNW–SSE striking normal fault zones present throughout the southern Ruhr area (Balcewicz et al. 2021), this observation is considered significant. Given the pervasive, fracture-bound nature of the dolomitisation, a clear assignment of carbonate precursor facies and degree of dolomitisation was not possible. Other work however (see Krebs 1974), stated that dolomitisation preferably occurs in fine-grained, micritic sections of the Schwelm Facies and the back-reef subtype of the Dorp Facies. Krebs (1974) did not specify if he refers to early diagenetic fabric preserving or late diagenetic, hydrothermal dolomitisation.

With increasing volumetric abundance of dolostone, the geothermal reservoir potential increases from a thermal property standpoint, due to an increase in the mean thermal conductivity. The thermal conductivity of a given rock mainly depends on two factors: (i) the porosity – given that elevated pore space volumes lead to decreased thermal conductivities of the bulk sample due to the low thermal conductivity of air (or a hydrous fluid) compared to minerals – and (ii) the mineralogy (Francl & Kingery 1954; Robertson 1988). The total porosity values of the Devonian carbonates in the Steltenberg quarry display an inverse relationship with thermal conductivity and dolomite content (Fig. 6). According to Robertson (1988), the thermal conductivity of dolomite is higher compared to that of calcite (by up to  $4 \text{ Wm}^{-1}\text{K}^{-1}$ ). Hence, the volume of open pore space and the carbonate mineralogy both result in elevated  $\lambda$ -values in the case of dolostones.

The relationship between hydraulic properties and carbonate diagenesis are highly complex, given that these correlations depend on many superimposed factors. This complexity is documented in Fig. 10, illustrating the paragenetic sequence and associated diagenetic phases, and their influence on hydraulic properties. However, the authors note that plugs with fractures cutting through both end-faces of the cylindrical specimen have not been investigated in the context of this study, and hence, no quantitative trend of hydraulic parameters in relation of dolomite content is documented here (Fig. 6). Future work to better address the hydraulic properties in the quarry could include in-situ hydraulic testing. Pure limestone samples exhibit the highest mean porosity and the second-highest mean permeability values. Consequently, as opposed to dolostones, limestones are, from the viewpoint of geothermal reservoir research, the most promising mineralogy in the Steltenberg quarry – or so it seems in a first approximation. We wish to point out, however, that even what we refer to as limestones (Figs. 3, 6, 9), are in fact composite materials containing variable amounts of dolomite. Moreover, dolostones generally exhibit higher fracture densities compared to limestones (Korneva et al. 2018), indicating that fractured dolostones yield better hydraulic properties.

In conclusion, different areas of the Steltenberg quarry and the corresponding rocks, have experienced differential diagenetic and tectonic pathways leading to spatially complex distribution patterns of limestone and dolostone as well as intermediate lithologies. Each pathway resulted in a different effect on porosity and permeability, and therefore a range of hydraulic patterns that is spatially highly complex. Clearly, this is a warning to not oversimplify the spatial variability in subsurface reservoirs. This becomes particularly evident when extrapolating information from one or a limited number of core(s) across a km-scale rock body. Clearly, when referring to dolomitisation, the nature and timing of this diagenetic process must be considered. Further, it is important to separate between: (i) diffuse, locally distributed dolomitisation, (ii) replacive dolomitisation (fronts), spatially separating lime- and dolostones, and (iii) fault-bound, hydrothermal dolomitisation. Acknowledging these limitations, the value of large-scale outcrops is, in the view of the authors, undisputed.

#### 5.4 Comparison of Devonian (Hagen) and Jurassic (Munich) geothermal rock properties

The thermal and hydraulic parameters presented here can be compared to the petrophysical properties of the Malm (Upper Jurassic) carbonates in the Munich area. There, karstified geothermal carbonate reservoirs have been successfully exploited for decades (Dirner & Steiner 2015). As these karst features are of high importance in the geothermal potential of the Malm carbonates, further work could investigate the possibility of similar features in the subsurface Devonian carbonates of NRW. The focus must be on Palaeozoic (and perhaps Mesozoic) karstification that is expected to affect carbonates independent of their present burial depth. Table 3 shows the comparison of the mean values of the study in Hagen and in the Molasse Basin in Bavaria based on Homuth (2014). Although differences in the facies properties and the diagenetic and burial pathways between these two case examples limit a simple correlation, the petrophysical and hydraulic properties documented here seem promising. On average, the dolomitised Devonian carbonates in the Steltenberg quarry exhibit higher thermal conductivities compared to the Jurassic ones in the Munich area, with the limestone samples from Hagen also plotting above the

values of the basinal limestone facies of the Munich area (Table 3). Furthermore, the Devonian carbonates in the Steltenberg quarry show high total porosity values compared to those of the basin facies determined by Homuth (2014), while the porosity of the limestones and dolomitic limestones in Hagen exceeds those of the massive facies of the Malm carbonates. The permeability values of Devonian (Hagen) and Jurassic (Munich) reservoir rocks are within the same range. The partly dolomitised limestones of the Steltenberg quarry exhibit the highest permeability of all reported facies types in both case studies. Depositional facies-related petrophysical studies using thin sections from every plug analysed for thermal and hydraulic properties have the potential to increase the comparability of Devonian reservoir rocks to the Jurassic ones in the Munich area, and should be considered for future work. Furthermore, in combination with an understanding of the tectonic history and any recent reactivation of fault structures, hydraulic testing of deep and shallow faulted and non-faulted successions can help to better assess overall reservoir permeability.

## 6. Conclusions

Devonian carbonates as exposed in the Steltenberg quarry near Hagen (North Rhine-Westphalia) were analysed to provide insight to the depositional and diagenetic progression of the rock units, and to be used as an analogue for similar units in the subsurface with the potential for deep geothermal energy production. These outcrops are particularly suitable as they expose a regional fault zone providing access to a wide range of rocks and fabrics exposed to tectonic and hydrothermal overprint. A very diverse range of data is shown here, which documents that it is the combination of these approaches that results in a solid understanding of the complexity of the features studied here. Stratigraphic and petrographic analyses indicate a predominance of reefal Dorp and bank/platform Schwelm facies within the carbonate units, with large variations of diagenetic overprint. Both major and minor faults cut through the studied section, which experienced multiple phases of activation and the circulation of hydrothermal fluids through the host rock. This resulted in large scale geochemical and textural alteration within the fault core and damage zone, and a complicated paragenetic sequence that includes alteration in both the meteoric and

**Table 3:** Facies-related comparison of mean petrophysical values of carbonate units from the Munich area and the Steltenberg quarry in Hagen gained in outcrop analogue studies examining the deep geothermal reservoir potential (after Homuth 2014). See supplementary tables for all corresponding data and standard deviations.

	Munich (Homuth 2014)		Steltenberg quarry Hagen (this study)		
	Basin facies	Massive facies	Limestone	Dolomitic limestone	Dolostone
Thermal conductivity $\lambda$ (W m <sup>-1</sup> K <sup>-1</sup> )	1.9	2.6	2.3	2.8	3.3
Total porosity $\phi_{tot}$ (%)	3.5	6.0	10.8	6.0	5.1
Permeability $k$ (m <sup>2</sup> )	$5.0 \times 10^{-17}$	$1.0 \times 10^{-16}$	$6.7 \times 10^{-17}$	$3.5 \times 10^{-16}$	$3.4 \times 10^{-17}$

burial zone. Alteration processes resulted in a large variation of petrophysical characteristics and corresponding fluid flow potential. Although recrystallised, units further from the fault core display geochemical values similar to their depositional values, possibly indicating relatively early and shallow burial alteration. This study indicates geothermal reservoir potential based on comparison with reported data from a currently exploited reservoir in the Malm facies in the Munich area, but warrants further work in assessing fault zone permeability to better predict hydraulic productivity. The authors stress the documented high variability within the units due to differential alteration, and the necessity for correlation of as many properties of carbonate rocks as possible.

## 7. Acknowledgements

This study was supported by the Interreg NWE Programme through the Roll-out of Deep Geothermal Energy in North-West Europe (DGE-ROLLOUT) Project ([www.nweurope.eu/DGE-Rollout](http://www.nweurope.eu/DGE-Rollout)). The Interreg NWE Programme is part of the European Cohesion Policy and is financed by the European Regional Development Fund (ERDF). Further funding was provided by the Bundesministerium für Wirtschaft und Energie of NRW and the Ruhr-University Bochum Research Department under the Closed Carbon Cycle Economy project. We also thank the operators of the quarry, Christian Lange and Matthias A. Lange as CEOs of the Hohenlimburger Kalkwerke GmbH for access to the study site. Mathias Nehler, Martin Balcewicz, Kathrin Krimmler and Beate Gehnen are also thanked for their assistance in laboratory analyses. Furthermore, the authors thank the handling editor Martin Arndt, reviewer Kristian Bär, and one anonymous reviewer for their comments and efforts on the manuscript.

## 8. References

- Agosta, F., & Aydin, A. (2006). Architecture and deformation mechanism of a basin-bounding normal fault in Mesozoic platform carbonates, central Italy. *Journal of Structural Geology*, 28(8), 1445–1467. <https://doi.org/10.1016/j.jsg.2006.04.006>
- Agosta, F., Ruano, P., Rustichelli, A., Tondi, E., Galindo-Zaldívar, J., & Sanz de Galdeano, C. (2012). Inner structure and deformation mechanisms of normal faults in conglomerates and carbonate grainstones (Granada Basin, Betic Cordillera, Spain): Inferences on fault permeability. *Journal of Structural Geology*, 45, 4–20. <https://doi.org/10.1016/j.jsg.2012.04.003>
- Balcewicz, M., Ahrens, B., Lippert, K., & Saenger, E. H. (2021). Characterization of discontinuities in potential reservoir rocks for geothermal applications in the Rhine-Ruhr metropolitan area (Germany). *Solid Earth*, 12(1), 35–58. <https://doi.org/10.5194/se-12-35-2021>
- Barbier, M., Hamon, Y., Callot, J. P., Floquet, M., & Daniel, J. M. (2012). Sedimentary and diagenetic controls on the multiscale fracturing pattern of a carbonate reservoir: The Madison Formation (Sheep Mountain, Wyoming, USA). *Marine and Petroleum Geology*, 29(1), 50–67. <https://doi.org/10.1016/j.marpetgeo.2011.08.009>
- Beckmann, H. (1948). Mikrofaunen von der Mitteldevon-Oberdevongrenze im nördlichen Sauerland. *Doctoral dissertation University of Marburg*.
- Billi, A., Salvini, F., & Storti, F. (2003). The damage zone-fault core transition in carbonate rocks: Implications for fault growth, structure and permeability. *Journal of Structural Geology*, 25(11), 1779–1794. [https://doi.org/10.1016/S0191-8141\(03\)00037-3](https://doi.org/10.1016/S0191-8141(03)00037-3)
- Birck, J. L. (1986). Precision K-Rb-Sr isotopic analysis: Application to Rb-Sr chronology. *Chemical Geology*, 56(1–2), 73–83. [https://doi.org/10.1016/0009-2541\(86\)90111-7](https://doi.org/10.1016/0009-2541(86)90111-7)
- Bjørlykke, K. (2014). Relationships between depositional environments, burial history and rock properties. Some principal aspects of diagenetic process in sedimentary basins. *Sedimentary Geology*, 301, 1–14. <https://doi.org/10.1016/j.sedgeo.2013.12.002>
- Bohnsack, D., Potten, M., Pfrang, D., Wolpert, P., & Zosseder, K. (2020). Porosity-permeability relationship derived from Upper Jurassic carbonate rock cores to assess the regional hydraulic matrix properties of the Malm reservoir in the South German Molasse Basin. *Geothermal Energy*, 8(12), 1–47. <https://doi.org/10.1186/s40517-020-00166-9>
- Bruckschen, P., & Richter, D. K. (1993). Zementstratigraphische Grundmuster in marinen Karbonatablagerungen des Phanerozoikums – Ein Abbild der normalen Beckenentwicklung. *Zentralblatt für Geologie und Paläontologie, Teil I: Allgemeine, Angewandte, Regionale und Historische Geologie*, 7–8, 959–972.
- Bruckschen, P., Neuser, R. D., & Richter, D. K. (1992). Cement stratigraphy in Triassic and Jurassic limestones of the Weserbergland (northwestern Germany). *Sedimentary Geology*, 81(3–4), 195–214. [https://doi.org/10.1016/0037-0738\(92\)90070-8](https://doi.org/10.1016/0037-0738(92)90070-8)
- Burchette, T. P. (1981). European Devonian reefs: A review of current concepts and models. *Special Publication - Society of Economic Paleontologists and Mineralogists*, 30, 85–142. <https://doi.org/10.2110/pec.81.30.0085>
- Caine, J. S., Evans, J. P., & Forster, C. B. (1996). Fault zone architecture and permeability structure. *Geology*, 24(11), 1025–1028. [https://doi.org/10.1130/0091-7613\(1996\)0242.3.CO;2](https://doi.org/10.1130/0091-7613(1996)0242.3.CO;2)
- Chester, F. M., & Logan, J. M. (1986). Implications for mechanical properties of brittle faults from observations of the Punchbowl fault zone, California. *Pure and Applied Geophysics*, 124(1–2), 79–106. <https://doi.org/10.1007/BF00875720>
- Choi, J. H., Edwards, P., Ko, K., & Kim, Y. S. (2016). Definition and classification of fault damage zones: A review and a new methodological approach. *Earth-Science Reviews*, 152, 70–87. <https://doi.org/10.1016/j.earscirev.2015.11.006>
- Darcy, H. (1856). *The public fountains of the city of Dijon*. Paris: Victor Dalmont.
- Davatzes, N. C., & Aydin, A. (2003). The formation of conjugate normal fault systems in folded sandstone by sequential jointing and shearing, Waterpocket monocline, Utah. *Journal of Geophysical Research*, 108(B10), 1–15. <https://doi.org/10.1029/2002JB002289>
- Davatzes, N. C., Eichhubl, P., & Aydin, A. (2005). Structural evolution of fault zones in sandstone by multiple deformation mechanisms: Moab fault, southeast Utah. *Geological Society of America Bulletin*, 117(1–2), 135–148. <https://doi.org/10.1130/B25473.1>
- Davies, G. R., & Smith, L. B., Jr. (2006). Structurally controlled hydrothermal dolomite reservoir facies: An overview. *AAPG Bulletin*, 90(11), 1641–1690. <https://doi.org/10.1306/05220605164>
- DIN ISO 18124 (2019). Soil, investigation and testing – Determination of density of solid particles – Wide mouth pycnometer.
- Dirner, S., & Steiner, U. (2015). Assessing reservoir uncertainty with stochastic facies modeling of a hydrothermal medium en-

- thalpy reservoir (Upper Jurassic Carbonates of the Southern German Molasse Basin). *International Geothermal Association, Proceedings World Geothermal Congress Melbourne*.
- Drozdowski, G., & Wrede, V. (1994). Faltung und Bruchtektonik – Analyse der Tektonik im Subvariszikum. *Fortschritte in der Geologie von Rheinland und Westfalen*, 38, 7–187.
- Dunham, R. J. (1962). Classification of carbonate rocks according to depositional texture. In W. E. Ham (Ed.), *Classification of carbonate rocks* (pp. 108–121). Tulsa: AAPG.
- Eberli, G. P., Baechle, G. T., Anselmetti, F. S., & Incze, M. L. (2003). Factors controlling elastic properties in carbonate sediments and rocks. *The Leading Edge*, 22(7), 654–660. <https://doi.org/10.1190/1.1599691>
- Faulkner, D. R., Jackson, C. A. L., Lunn, R. J., Schlische, R. W., Sipton, Z. K., Wibberley, C. A. J., & Withjack, M. O. (2010). A review of recent developments concerning the structure, mechanics and fluid flow properties of fault zones. *Journal of Structural Geology*, 32(11), 1557–1575. <https://doi.org/10.1016/j.jsg.2010.06.009>
- Federal Agency for Cartography and Geodesy (2020). Geographie, Geologie und Geobasisdaten. Retrieved from <https://www.geoportal.nrw/>
- Francl, J., & Kingery, W. D. (1954). Thermal conductivity: IX, Experimental investigation of effect of porosity on thermal conductivity. *Journal of the American Ceramic Society*, 37(2), 99–107. <https://doi.org/10.1111/j.1551-2916.1954.tb20108.x>
- Franke, W., Bortfeld, R. K., Brix, M., Drozdowski, G., Dürbaum, H. J., Giese, P., . . . Wong, H. K. (1990). Crustal structure of the Rhenish Massif: Results of deep seismic reflection lines DE-KORP 2-North and 2-North-Q. *Geologische Rundschau*, 79(3), 523–566. <https://doi.org/10.1007/BF01879201>
- Frech, F. (1888). Geologie der Umgebung von Haiger bei Dillenburg (Nassau). *Abhandlungen der Königlich Preussischen Geologischen Landesanstalt*, 8(3), 223–258.
- Gillhaus, A., Götte, T., & Richter, D. K. (2003). Polyphase spätdiagenetische Dolomitbildung im mittel- bis oberdevonischen Massenkalk von Hagen-Hohenlimburg (Remscheid-Altener Sattel, Rheinisches Schiefergebirge). *Mitteilungen der Gesellschaft der Geologie- und Bergbaustudenten in Österreich*, 46, 51–66.
- Götte, T. (2004). Petrographische und geochemische Untersuchungen zu den postvariszischen Mineralisationen im devonischen Massenkalk des nordwestlichen Rechtsrheinischen Schiefergebirges unter besonderer Berücksichtigung der Kathodolumineszenz. *Dissertation University of Bochum* (186 pp.).
- Grabert, H. (1998). *Abriß der Geologie von Nordrhein-Westfalen*. Stuttgart: Schweizerbart.
- Grammer, G. M., Harris, P. M. M., & Eberli, G. P. (2004). Integration of outcrop and modern analogs in reservoir modeling: Overview with examples from the Bahamas. *AAPG Memoir*, 80(80), 1–22. <https://doi.org/10.1306/M80924C1>
- Grossman, E. L. (2012). Applying oxygen isotope paleothermometry in deep time. *The Paleontological Society Papers*, 18, 39–68. <https://doi.org/10.1017/S1089332600002540>
- Gunter, G. W., Finneran, J. M., Hartmann, D. J., & Miller, J. D. (1997). Early determination of reservoir flow units using an integrated petrophysical method. *Paper Number: SPE-38679-MS, Society of Petroleum Engineers annual technical conference and exhibition, San Antonio, Texas, October 1997*.
- Hammerschmidt, E., Niggemann, S., Grebe, W., Oelze, R., Brix, M. R., & Richter, D. K. (1995). Höhlen in Iserlohn. *Schriften zur Karst- und Höhlenkunde in Westfalen*, 1, 1–182.
- Hesemann, J. (1975). *Geologie Nordrhein-Westfalens*. Paderborn: Schoeningh.
- Homuth, S. (2014). Aufschlussanalogstudie zur Charakterisierung oberjurassischer geothermischer Karbonatreservoirs im Molassebecken. *Doctoral dissertation University Darmstadt* (314 pp.).
- Homuth, S., Götz, A. E., & Sass, I. (2014). Lithofacies and depth dependency of thermo- and petrophysical rock parameters of the Upper Jurassic geothermal carbonate reservoirs of the Molasse Basin. *Zeitschrift der Deutschen Gesellschaft für Geowissenschaften*, 165(3), 469–486. <https://doi.org/10.1127/1860-1804/2014/0074>
- Homuth, S., Götz, A. E., & Sass, I. (2015a). Physical properties of the geothermal carbonate reservoirs of the Molasse Basin, Germany – Outcrop analogue vs. reservoir data. *World Geothermal Congress 2015, Melbourne, Australia* (pp. 19–24).
- Homuth, S., Götz, A. E., & Sass, I. (2015b). Reservoir characterization of the Upper Jurassic geothermal target formations (Molasse Basin, Germany): role of thermofacies as exploration tool. *Geothermal Energy Science*, 3(1), 41–49. <https://doi.org/10.5194/gtes-3-41-2015>
- Howarth, R. J., & McArthur, J. M. (1997). Statistics for strontium isotope stratigraphy: A robust LOWESS fit to the marine Sr-isotope curve for 0 to 206 Ma, with look-up table for derivation of numeric age. *The Journal of Geology*, 105(4), 441–456. <https://doi.org/10.1086/515938>
- Hu, L., Winterfeld, P. H., Fakcharoenphol, P., & Wu, Y. S. (2013). A novel fully-coupled flow and geomechanics model in enhanced geothermal reservoirs. *Journal of Petroleum Science Engineering*, 107, 1–11. <https://doi.org/10.1016/j.petrol.2013.04.005>
- Igbokwe, O. A., Mueller, M., Bertotti, G., Timothy, J. J., Abah, O., & Immenhauser, A. (2020). Morphology and topology of dolostone lithons in the regional Carboneras Fault Zone, Southern Spain. *Journal of Structural Geology*, 137, 104073. <https://doi.org/10.1016/j.jsg.2020.104073>
- Jourde, H., Flodin, E. A., Aydin, A., Durlofsky, L. J., & Wen, X. H. (2002). Computing permeability of fault zones in eolian sandstone from outcrop measurements. *AAPG Bulletin*, 86(7), 1187–1200.
- Kaltschmitt, M., Streicher, W., & Wiese, A. (Hrsg.) (2006). *Erneuerbare Energien*. Berlin: Springer. <https://doi.org/10.1007/3-540-28205-X>
- Kamp, H. von (1968). 120. Hauptversammlung der Deutschen Geologischen Gesellschaft in Hagen Westfalen. *Exkursionsführer*, 21–22.
- Kayser, E. (1907). *Erläuterungen und Karte Blatt Dillenburg (5215), Geologische Karte von Preußen, Lieferung 101* (119 pp.).
- Kim, Y. S., Peacock, D. C., & Sanderson, D. J. (2004). Fault damage zones. *Journal of Structural Geology*, 26(3), 503–517. <https://doi.org/10.1016/j.jsg.2003.08.002>
- Kirnbauer, T. (Hrsg.) (1998). *Geologie und hydrothermale Mineralisationen im rechtsrheinischen Schiefergebirge, Sonderband 1*. Wiesbaden: Nassauischer Verein für Naturkunde.
- Knutzen, L. K., Stolpe, H., Bracke, R., & Beese, E. (2015). Conversion of conventional district heating systems in the Ruhr-Metropolitan Area, Western Germany, by stepwise integration of geothermal sources. *Proceedings World Geothermal Congress, Melbourne, Australia*, 19–25 April 2015.
- Koch, L., Voigt, S., & Brauckmann, C. (2018). Nautiliden aus der Kluterhöhle (Ennepetal, Nordrhein-Westfalen), aus benachbarten Höhlen und weiteren Fundorten in Oberen Honsel-

- Schichten (Unter-Givetium). *Geologie und Paläontologie in Westfalen*, 90, 15–24.
- Koch-Früchtel, U., & Früchtel, M. (1993). Stratigraphie und Faziesanalyse einer mitteldevonischen Karbonatabfolge im Remscheid-Altenaer Sattel (Sauerland). *Geologie und Paläontologie in Westfalen*, 26, 47–75.
- Korneva, I., Bastesen, E., Corlett, H., Eker, A., Hirani, J., Hollis, C., . . . Taylor, R. (2018). The effects of dolomitization on petrophysical properties and fracture distribution within rift-related carbonates (Hammam Faraun Fault Block, Suez Rift, Egypt). *Journal of Structural Geology*, 108, 108–120. <https://doi.org/10.1016/j.jsg.2017.06.005>
- Krebs, W. (1967). Reef development in the Devonian of the eastern Rhenish Slate Mountains, Germany. In D. H. Oswald (Ed.), *International Symposium on the Devonian System, Calgary 1967*, 2, 295–306.
- Krebs, W. (1974). Devonian carbonate complexes of Central Europe. In L. F. Laporte (Ed.), *Reefs in time and space. Society of Economic Palaeontologists and Mineralogists, Special Publication*, 18, 155–208. <https://doi.org/10.2110/pec.74.18.0155>
- Lippert, K., Nehler, M., Balcewicz, M., Bracke, R., & Immenhauser, A. (2019). Facies-related evaluation of the geothermal reservoir potential of Devonian carbonates in North Rhine-Westphalia, Germany. *81<sup>st</sup> EAGE Conference and Exhibition 2019, June 2019. Conference Proceedings 2019*, 1–5.
- Littke, R., Bükler, C., Hertle, M., Karg, H., Stroetmann-Heinen, V., & Oncken, O. (2000). Heat flow evolution, subsidence and erosion in the Rheno-Hercynian orogenic wedge of central Europe. In W. Franke, V. Haak, O. Oncken, & D. Tanner (Eds.), *Orogenic processes: Quantification and modelling in the Variscan Belt. Special Publication – Geological Society of London*, 179, 231–255. <https://doi.org/10.1144/GSL.SP.2000.179.01.15>
- Manger, E. (1963). Porosity and bulk density of sedimentary rocks. *Contributions to Geochemistry. Geological Survey Bulletin*, 1144-E. <https://pubs.usgs.gov/bul/1144e/report.pdf>
- Manzocchi, T. (2002). The connectivity of two-dimensional networks of spatially correlated fractures. *Water Resources Research*, 38(9), 1–20. <https://doi.org/10.1029/2000WR000180>
- Maxwell, S. C., Cho, D., Pope, T. L., Jones, M., Cipolla, C. L., Mack, M. G., . . . Leonard, J. A. (2011). Enhanced reservoir characterization using hydraulic fracture microseismicity. *SPE Hydraulic Fracturing Technology Conference. Society of Petroleum Engineers*. <https://doi.org/10.2118/140449-MS>
- Meier, S., Bauer, J. F., & Philipp, S. L. (2017). Fault zones in layered carbonate successions: from field data to stress field models. *Geomechanics and Geophysics for Geo-Energy and Geo-Resources*, 3(1), 61–93. <https://doi.org/10.1007/s40948-016-0047-x>
- Mueller, C., Siegesmund, S., & Blum, P. (2010). Evaluation of the representative elementary volume (REV) of a fractured geothermal sandstone reservoir. *Environmental Earth Sciences*, 61(8), 1713–1724. <https://doi.org/10.1007/s12665-010-0485-7>
- Mueller, M. (2020). Assessing the reliability of dolostones as palaeoenvironmental archives. *Doctoral dissertation University of Bochum* (261 pp.).
- Mueller, M., Igbokwe, O. A., Walter, B., Pederson, C. L., Riechelmann, S., Richter, D. K., . . . Immenhauser, A. (2020). Testing the preservation potential of early diagenetic dolomites as geochemical archives. *Sedimentology*, 67(2), 849–881. <https://doi.org/10.1111/sed.12664>
- Neuser, R. D., Bruhn, F., Götze, J., Habermann, D., & Richter, D. K. (1996). Kathodolumineszenz: Methodik und Anwendung. *Zentralblatt für Geologie und Paläontologie, Teil I*, 1995, 287–306.
- Nyberg, B., Nixon, C. W., & Sanderson, D. J. (2018). NetworkGT: A GIS tool for geometric and topological analysis of two-dimensional fracture networks. *Geosphere*, 14(4), 1618–1634. <https://doi.org/10.1130/GES01595.1>
- Oncken, O. (1988). Aspects of the reconstruction of the stress history of a fold and thrust belt (Rhenish Massif, Federal Republic of Germany). *Tectonophysics*, 152(1–2), 19–40. [https://doi.org/10.1016/0040-1951\(88\)90027-3](https://doi.org/10.1016/0040-1951(88)90027-3)
- Paeckelmann, W. (1913). Das Oberdevon des Bergischen Landes. *Abhandlungen der Preußischen Geologischen Landesanstalt*, 70, 1–365.
- Pederson, C. L., Mavromatis, V., Dietzel, M., Rollion-Bard, C., Breitenbach, S. F. M., Yu, D., . . . Immenhauser, A. (2020). Variation in the diagenetic response of aragonite archives to hydrothermal alteration. *Sedimentary Geology*, 406, 105716. <https://doi.org/10.1016/j.sedgeo.2020.105716>
- Popov, Y. A., Semionov, V. G., Korosteliov, V. M., & Berezin, V. V. (1983). Non-contact evaluation of thermal conductivity of rocks with the aid of a mobile heat source. *Izvestiya. Physics of the Solid Earth*, 19, 563–567.
- Radke, B. M., & Mathis, R. L. (1980). On the formation and occurrence of saddle dolomite. *Journal of Sedimentary Research*, 50(4), 1149–1168.
- Richter, D. (1995). *Ruhrgebiet und Bergisches Land – Zwischen Ruhr und Wupper*. Sammlung geologischer Führer, 55 (222 pp.). Berlin: Borntraeger.
- Richter, D. K. (2000). Die Eifeler Nord-Süd Zone: Vom Devonmeer zur Kluterthöhle. *Bochumer Geologische und Geotechnische Arbeiten*, 55, 205–225.
- Richter, D. K., Götze, T., Götze, J., & Neuser, R. D. (2003). Progress in application of cathodoluminescence (CL) in sedimentary petrology. *Mineralogy and Petrology*, 79(3), 127–166. <https://doi.org/10.1007/s00710-003-0237-4>
- Robertson, E. C. (1988). Thermal properties of rocks. *U.S. Geological Survey Open-File Report*, 88–441, 1–110.
- Rosenfeld, U. (1961). Der Massenkalk des nördlichen Sauerlandes. *Mitteilungen des Verbandes der Deutschen Höhlen- und Karstforscher*, 7, 41–64.
- Rustichelli, A., Tondi, E., Agosta, F., Cilona, A., & Giorgioni, M. (2012). Development and distribution of bed-parallel compaction bands and pressure solution seams in carbonates (Bolognano Formation, Majella Mountain, Italy). *Journal of Structural Geology*, 37, 181–199. <https://doi.org/10.1016/j.jsg.2012.01.007>
- Salamon, M., Fritschle, T., & Thiel, A. (2020). *Bohrprognose Hagen Kabel*. Krefeld: Geologischer Dienst NRW.
- Saltzman, M. R., & Thomas, E. (2012). Carbon isotope stratigraphy. In F. M. Gradstein, J. G. Ogg, M. Schmitz, & G. Ogg (Eds.), *The geologic time scale*, 1, 207–232. <https://doi.org/10.1016/B978-0-444-59425-9.00011-1>
- Sanderson, D. J., & Nixon, C. W. (2015). The use of topology in fracture network characterization. *Journal of Structural Geology*, 72, 55–66. <https://doi.org/10.1016/j.jsg.2015.01.005>
- Sanderson, D. J., & Nixon, C. W. (2018). Topology, connectivity and percolation in fracture networks. *Journal of Structural Geology*, 115, 167–177. <https://doi.org/10.1016/j.jsg.2018.07.011>
- Shinn, E. A., & Robbin, D. M. (1983). Mechanical and chemical compaction in fine-grained shallow-water limestones. *Journal of Sedimentary Research*, 53(2), 595–618.

- Sibley, D. F., & Gregg, J. M. (1987). Classification of dolomite rock textures. *Journal of Sedimentary Research*, 57(6), 967–975.
- Sibson, R. H. (1977). Fault rocks and fault mechanisms. *Journal of the Geological Society*, 133(3), 191–213. <https://doi.org/10.1144/gsjgs.133.3.0191>
- Stober, I. (2014). Hydrochemical properties of deep carbonate aquifers in the SW German Molasse basin. *Geothermal Energy*, 2(1), 1–20. <https://doi.org/10.1186/s40517-014-0013-1>
- Swart, P. K. (2015). The geochemistry of carbonate diagenesis: The past, present and future. *Sedimentology*, 62(5), 1233–1304. <https://doi.org/10.1111/sed.12205>
- Tan, F., Zhao, R., Zhao, Y., Pan, Z., & Li, H. (2017). A case study: Evaluating low-porosity and ultra-low-permeability Triassic reservoir rocks in the Ordos Basin by the integration of logs and core. *Petroleum Geoscience*, 23(4), 454–465. <https://doi.org/10.1144/petgeo2016-146>
- Thiel, A. (2018). *Tiefenmodell NRW. Data license Germany version 2.0*. Krefeld: Geologischer Dienst NRW.
- Thome, K. N. (1970). Die Bedeutung der Ennepe-Störung für die Sedimentations und Faltungsgeschichte des Rheinischen Schiefergebirges. *Fortschritte in der Geologie von Rheinland und Westfalen*, 17, 757–808.
- Ti, G., Ogbe, D. O., Munly, W., & Hatzignatiou, D. G. (1995). The use of flow units as a tool for reservoir description: A case study. *SPE Formation Evaluation*, 10(2), 122–128. <https://doi.org/10.2118/26919-PA>
- Townend, J., & Zoback, M. D. (2000). How faulting keeps the crust strong. *Geology*, 28(5), 399–402. [https://doi.org/10.1130/0091-7613\(2000\)282.0.CO;2](https://doi.org/10.1130/0091-7613(2000)282.0.CO;2)
- Veizer, J., & Prokoph, A. (2015). Temperatures and oxygen isotopic composition of Phanerozoic oceans. *Earth-Science Reviews*, 146, 92–104. <https://doi.org/10.1016/j.earscirev.2015.03.008>
- Weydt, L. M., Bär, K., Colombero, C., Comina, C., Deb, P., Lepillier, B., . . . Sass, I. (2018). Outcrop analogue study to determine reservoir properties of the Los Humeros and Acoculco geothermal fields, Mexico. *Advances in Geosciences*, 45, 281–287. <https://doi.org/10.5194/adgeo-45-281-2018>
- Wissing, L. (2009). Germany Country Report. *21st IEA GIA ExCo Meeting, Madrid, Spain*.
- Yielding, G., Øverland, J. A., & Byberg, G. (1999). Characterization of fault zones for reservoir modeling: An example from the Gullfaks field, northern North Sea. *AAPG Bulletin*, 83(6), 925–951.

Manuscript received: 25.02.2021

Revisions required: 12.05.2021

Revised version received: 23.07.2021

Accepted for publication: 07.09.2021

## Electronic supplements

Supplementary material associated with this article is embedded in the pdf of this article. The online version of *Zeitschrift der Deutschen Gesellschaft für Geowissenschaften – Journal of Applied and Regional Geology (ZdGG)* is hosted at the journal's website [www.schweizerbart.com/journals/zdgg](http://www.schweizerbart.com/journals/zdgg). The publisher does not bear any liability for the lack of usability or correctness of supplementary material.

**Supplementary Tables:** The tables show all sedimentological, petrographic, petrophysical, and geochemical corresponding data mentioned in the manuscript.

Please save the electronic supplement contained in this pdf-file by clicking the blue frame above. After saving rename the file extension to .zip (for security reasons Adobe does not allow to embed .exe, .rar etc. files).